How well are aerosol-cloud interactions represented in climate models? Part 1: Understanding the sulphate aerosol production from the 2014-15 Holuhraun eruption.

George Jordan[1], Jim Haywood[1,2], Florent Malavelle[3], Ying Chen[4], Amy Peace[2], Eliza Duncan[2], Daniel G. Partridge[2], Paul Kim[2], Duncan Watson-Parris[5], Toshihiko Takemura[6], David Neubauer[7], Gunnar Myhre[8], Ragnhild Skeie[8] and Anton Laakso[9]

[1] Met Office Hadley Centre, Exeter, UK
[2] College of Engineering, Mathematics, and Physical Sciences, University of Exeter, Exeter, UK
[3] Met Office, Exeter, UK
[4] Laboratory of Atmospheric Chemistry, Paul Scherrer Institute, Switzerland
[5] Scripps Institution of Oceanography and Halicioğlu Data Science Institute, University of California San Diego, La Jolla, CA, USA
[6] Kyushu University, Fukuoka, Japan
[7] Institute for Climate and Atmospheric Science, ETH Zurich, Zurich, Switzerland
[8] CICERO Center for International Climate and Environmental Research, Oslo, Norway
[9] Finnish Meteorological Institute, Atmospheric Research Centre of Eastern Finland, Kuopio, Finland

Correspondence to: George Jordan (george.jordan@metoffice.gov.uk)

Abstract. For over 6-months, the 2014–2015 effusive eruption at Holuhraun, Iceland injected considerable amounts of sulphur dioxide (SO_2) into the lower troposphere with a daily rate of up to one-third of the global emission rate causing extensive air pollution across Europe. The large injection of SO_2, which oxidises to form sulphate aerosol (SO_4^{2-}), provides a natural experiment offering an ideal opportunity to scrutinise state-of-the-art general circulation models (GCMs) representation of aerosol-cloud interactions (ACIs). Here we present Part 1 of a two-part model inter-comparison using the Holuhraun eruption as a framework to analyse ACIs. We use SO_2 retrievals from the Infrared Atmospheric Sounding Interferometer (IASI) instrument and ground-based measurements of SO_2 and SO_4^{2-} mass concentrations across Europe in conjunction with trajectory analysis using the Hybrid Single Particle Lagrangian Integrated Trajectory (HYSPLIT) model to assess the spatial and chemical evolution of the volcanic plume as simulated by 5 GCMs and a chemical transport model (CTM). IASI retrievals of plume altitude and SO_2 column load reveal that the volcanic perturbation is largely contained within the lower troposphere and that the spatial evolution and vertical variability of the plume is reasonably well captured by the models, although the models underestimate the mean plume altitude. HYSPLIT trajectories are used to attribute to Holuhraun emissions 184 instances of elevated sulphurous surface mass concentrations recorded at 22 air monitoring stations across Europe. Comparisons with the simulated concentrations show that the models underestimate the elevated SO_2 concentrations observed at stations closer to Holuhraun whilst overestimating those observed further away. Using a biexponential function to describe the decay of observed surface mass concentration ratios of SO_2-to-SO_4^{2-} with plume age,

35   in-plume gas-phase and aqueous-phase oxidation rates are estimated as 0.031 ± 0.002 h^{-1} and 0.22 ± 0.16 h^{-1} respectively with a near-vent ratio of 31 ± 4 [µgm^{-3} of SO$_2$ / ugm^{-3} of SO$_4^{2-}$]. The derived gas-phase oxidation rates from the models are all lower than the observed estimate, whilst the majority of the aqueous-phase oxidation rates agree with the observed rate. This suggests that the simulated plumes capture the observed chemical behaviour in the young plume (when aqueous-phase oxidation is dominant), yet not in the mature plume (when gas-phase oxidation is dominant). Overall, despite their coarse

40   resolution, the 6 models show reasonable skill in capturing the spatial and chemical evolution of the Holuhraun plume which is essential when exploring the eruption impact on ACIs in the second part of this study.

1 Introduction

The Bárðarbunga volcanic system in Iceland began experiencing noteworthy sequences of earthquakes on 16th August 2014 (Ágústsdóttir et al., 2016; Gudmundsson et al., 2014; Sigmundsson et al., 2015). This seismic activity created an effusive

45   eruption at Holuhraun (64.85°N, 16.83°W) from 31st August 2014 to 27th February 2015. The resulting flow of lava is estimated to have covered 84 km^2 with an average discharge rate of 90 m^{3}s^{-1} making it the largest effusive eruption in Iceland since the 1783-1784 Laki eruption (Pedersen et al., 2017). Ground-based observation estimates suggest the Holuhraun eruption released a total of 9.6–11.8 Mt of sulphur dioxide (SO$_2$) with little tephra (Gíslason et al., 2015; Pfeffer et al., 2019). These emissions represent up to 215 times the amount of Icelandic anthropogenic SO$_2$ emissions for 2019 (Keller et al.,

50   2022) and approximately one tenth of the current global annual anthropogenic emissions (e.g. Aas et al., 2015). During these months of intense degassing, several studies using ground-based observations and remote sensing suggest that the volcanic plume reached altitudes of 1–4 km (Arason et al., 2015; Carboni et al., 2019a; Flower and Kahn 2020; Pfeffer et al., 2019). This release of SO$_2$ adversely affected air quality over large parts of Iceland often exceeding World Health Organization (WHO) surface concentration limits (Gíslason et al., 2015; Ilyinskaya et al., 2017; Schmidt et al., 2015). Such high rates of

55   SO$_2$ emission into a relatively pristine, unpolluted environment provide an ideal opportunity to observe aerosol aerosol-cloud interactions (ACIs) (e.g. Breen et al., 2021; Chen et al., 2022; Gettelman et al., 2015; Haghighatnasab et al., 2022; Malavelle et al., 2017, McCoy and Hartmann, 2015, Toll et al., 2017) and elucidate aerosol impacts on the climate system.

Remote sensing data estimates of SO$_2$ concentrations, a common tool to monitor the evolution of volcanic plumes, show that

60   the September and October meteorological conditions transported the plume across Europe including the Fennoscandian Peninsula (Grahn et al., 2015; Ialongo et al., 2015), Belgium, northern France (Boichu et al., 2016), the UK, Ireland, the Netherlands (Schmidt et al., 2015) and Germany (Steensen et al., 2016). Previous studies have combined satellite data with ground-based observations and trajectory modelling to attribute local pollution events to the Holuhraun eruption and investigate the plume characteristics (e.g. Boichu et al., 2019; Schmidt et al., 2015; Twigg et al., 2016). Understanding such

65   characteristics, particularly those that are hazardous to health i.e. such as fine particulate matter, is important for air quality monitoring and attribution of any exceedances of statutory thresholds (Heaviside et al. 2021; Stewart et al., 2022). However,

most studies that assessed Holuhraun impacts on air quality focus only on the pollution experienced at a few ground-based stations across small geographical areas and the need to expand the quantity of air monitoring stations used has been noted previously (Schmidt et al., 2015; Twigg et al., 2016).

70

In addition to the observational evidence, many studies have also used numerical modelling to simulate the transport of SO_2 emitted by the Holuhraun eruption. For instance, Iceland Meteorological Office employed the CALPUFF dispersion model for near-time probabilistic hazard mapping (Barsotti, 2020) and to support aviation safety decisions (Barsotti et al., 2020). Furthermore, Boichu et al. (2016) and Steensen et al. (2016) used the EMEP MSC-W and the CHIMERE chemical transport

75   models (CTMs) respectively to explore the far-range air pollution effects, whereas Schmidt et al. (2015) used the NAME dispersion model. Recently, Haghighatnasab et al. (2022) analysed the results from high resolution simulations performed with the ICON model in its numerical weather prediction mode to explore the impact of aerosols on cloud properties. This impact was also examined in earlier works using general circulation models (GCMs) of coarser resolutions (CAM5 – Gettelman et al., 2015; HadGEM3, CAM5, and a NorESM variant – Malavelle et al., 2017). Considering the opportunity the

80   Holuhraun eruption presents to assess the modelling capability of GCMs in capturing aerosol-cloud interactions, the number of GCM studies of the Holuhraun eruption to date is surprisingly low.

Here we present results from an inter-model comparison two-part study of the volcanic plume and its interactions with clouds within the vicinity of the Holuhraun eruption (44°N to 80°N, 60°W to 30°E) during September and October 2014.

85   Participation in the study was organised through the AeroCom initiative (Schulz et al., 2006). We begin with a comparison of the volcanic SO_2 plume evolution between remote sensing observations and simulations of the eruption from 5 GCMs and a CTM. The analysis specifically focuses on the plume spatial distribution, plume altitude and the total SO_2 mass burden. We further investigate the numerical models' capability to simulate the Holuhraun eruption by comparing modelled SO_2 and sulphate (SO_4^{2-}) concentrations with in situ surface observations from 25 long-term monitoring stations from the EMEP

90   (European Monitoring and Evaluation Programme) network. By using remote sensing and ground-based observations in conjunction with trajectory modelling, we can attribute pollution events dominated by sulphur to the Holuhraun emissions and assess the skills of the different numerical models in capturing these events. Finally, this refined catalogue of volcanically influenced pollution events is used to estimate the rate at which SO_2 oxidises to SO_4^{2-} within both observed and modelled volcanic plumes. We conclude with a discussion of whether the models simulate the observed perturbation with

95   sufficient fidelity; a prerequisite for understanding the climatic impacts of the Holuhraun eruption via ACIs (see Part 2 of this study).

2 Methodology

We provide a brief description of the remote sensing and in situ observations that are used to assess the numerical models, the numerical models themselves, and the HYSPLIT trajectory modelling framework used to estimate the origin and age of the observed local sulphurous pollution events.

2.1 Satellite Observations

Retrievals of volcanic SO_2 from satellite instrumentation typically use either measurements in the ultra-violet (e.g. Ozone Mapping and Profiler Suite – Nadir Mapper (OMPS-NM); Carn et al., 2015; Li et al., 2017; Wells et al., 2023; TROPOspheric Monitoring Instrument (TROPOMI); de Leeuw et al., 2021; Theys et al., 2017; Global Ozone Monitoring Experiment-2 (GOME-2); Twigg et al., 2016) or infra-red (e.g. Infrared Atmospheric Sounding Interferometer (IASI); Clarisse et al., 2008, 2010, Haywood et al., 2010, de Leeuw et al., 2021) region of the electromagnetic spectrum. Here we use IASI measurements as they have proved valuable in monitoring the evolution of volcanic plumes in both the stratosphere (e.g. Haywood et al., 2010; de Leeuw et al., 2021) and the troposphere (e.g. Athanassiadou et al., 2016; Malavelle et al., 2017). Specifically, we use data from IASI retrievals on the MetOp-A and MetOp-B satellites produced by the University of Oxford as part of the NERC Centre for the Observation and Modelling of Earthquakes, Volcanoes and Tectonics (COMET) (Carboni et al. 2019). SO_2 column load and plume height is derived by applying the IASI retrieval algorithm of Carboni et al. (2012, 2016) to level 1C data from the EUMETSAT and CEDA archive. The IASI SO_2 retrieval is performed only on pixels where the SO_2 detection is positive which in this scheme is explicitly defined as where the SO_2 column load > 0.49 Dobson units (DU). This detection threshold is based on the significance of a value in relation to the climatology whilst also accounting for the total retrieval error (Walker et al. 2011, 2012). The retrieval algorithm applied to these detected pixels uses all channels within 1000–1200 cm^{-1} and 1300–1410 cm^{-1} (the 7.3 μm and 8.7 μm SO_2 bands respectively) and assumes a Gaussian vertical SO_2 profile to return the SO_2 column load (DU) and height (mb) which is subsequently converted to km using meteorological temperature profiles. The algorithm provides a comprehensive pixel-by-pixel error estimate on the retrieved parameters (details in Carboni et al., 2012). The thermal contrast between the plume and surface heavily influences this error such that retrievals of SO_2 plumes centred at lower altitudes have higher uncertainties. This study groups the individual IASI orbits into bidaily intervals (AM: 00:00–12:00 UTC, PM: 12:00–24:00 UTC). Data from each group of orbits are resampled to a regular 0.125° x 0.125° grid using a nearest neighbours with Gaussian weighting approach with overlapping values averaged. The decision to weight closer neighbouring pixels allows retention of plume characteristics which can change abruptly over small spatial scales. Primarily the SO_2 retrievals from MetOp-A orbits are used, yet when coverage is sparse, those from MetOp-B are also used. Each bidaily regridded IASI SO_2 column load map is visually inspected to ensure no obvious artefacts exist. Note that the IASI retrieval algorithm can miss parts of the SO_2 plume, such as when overlaying clouds are present or under conditions of negative thermal contrast, and so the IASI SO_2 column loads and burdens presented here should be considered to be an approximate minimum.

2.2 Surface Observations

130   Since the early 1970s, the EMEP network has monitored air pollution and surface deposition across Europe at surface stations outside of significant conurbations that are only weakly affected by local pollution thus creating a comprehensive database useful for assessing long-range transportation of a plethora of pollutants (Tørseth et al., 2012). This study only considers EMEP stations that provide both SO_2 and SO_4^{2-} surface mass concentration measurements at the same temporal sampling during September and October 2014. The observations include hourly and daily measurements made using online

135   ion chromatography and filter-pack measurements respectively with the former to a precision of 0.001 μgm^{-3} and the latter to either 0.01 μgm^{-3} or 0.001 μgm^{-3}. Further details on the instruments and sampling techniques are provided in the EMEP Standard Operating Protocol (NILU, 2014). This study screens out invalid and missing measurements in accordance with the EMEP data quality flags (NILU, 2020). For each station monthly surface mass concentration climatologies for SO_2, SO_4^{2-} and combined total sulphur are calculated from the full temporal coverage available and used to assess significance. Here a

140   significant sulphurous pollution event is defined as when the surface mass concentration of the total sulphur content observed exceeds the 90th percentile of the corresponding monthly climatological value. Note that the number of EMEP stations carrying out SO_2 and SO_4^{2-} measurements has fallen since the late 2000s due to the reduced need to monitor the declining sulphur emissions from anthropogenic sources (Boichu et al., 2019; Schmidt et al., 2015). The 25 EMEP stations located across 12 countries selected for this study are listed in Table 1.

145

Station Name	Country	EMEP Station Code	Instrument Type/s	Freq.	Temporal Coverage	Lat. (N)	Lon. (E)	Alt. (m AMSL)	Trajectory Starting Height (m AGL)
Anholt	Denmark	DK0008R	Filter-3pack	Daily	1989-2020	56.71667	11.51667	40	100
Risoe	Denmark	DK0012R	Filter-3pack	Daily	2011-2020	55.69359	12.0858	3	100
Tange	Denmark	DK0003R	Filter-3pack Filter-2pack	Daily	1978-2020	56.35	9.6	13	100
Harwell	England	GB0036R	Online Ion Chroma.	Hourly	2009-2015 (SO_2 from 2011)	51.57306	-1.31667	137	100
Pallas Matorova	Finland	FI0036R	Filter-3pack Filter-2pack	Daily	1996-2020	68	24.23722	340	250
Utö	Finland	FI0009R	Filter-3pack Filter-2pack Filter-1pack	Daily	1980-2020 (SO_2 from 1991)	59.77917	21.37722	7	100
Virolahti II	Finland	FI0017R	Filter-3pack Filter-2pack	Daily	1989-2014 (SO_2 from 1991)	60.52667	27.68611	4	100
Neuglobsow	Germany	DE0007R	Filter-3pack Filter-1pack	Daily	1981-2018 (SO_2 from 2000)	53.16667	13.03333	62	100
Schauinsland	Germany	DE0003R	Filter-3pack	Daily	2000-2018	47.91472	7.90861	1205	550
Waldhof	Germany	DE0002R	Filter-3pack	Daily	2000-2018 (SO_4^{2-} from 2005)	52.80222	10.75944	74	100
Irafoss	Iceland	IS0002R	Filter-2pack Filter-1pack	Daily	1980-2020 (SO_2 from 2006)	64.08333	-21.01667	66	100
Valentia Observatory	Ireland	IE0001R	Filter-3pack Filter-2pack	Daily	1980-2020	51.93972	-10.24444	11	100
Rucava	Latvia	LV0010R	Filter-2pack Filter-1pack	Daily	1986-2020 (SO_2 from 1990)	56.16194	21.17306	18	100
Preila	Lithuania	LT0015R	Filter-3pack Filter-2pack	Daily	1991-2020 (SO_2 from 1996)	55.37611	21.03056	5	250
Birkenes II	Norway	NO0002R	Filter-3pack	Daily	2010-2020	58.38853	8.252	219	100
Hurdal	Norway	NO0056R	Filter-3pack	Daily	1997-2020	60.37239	11.07814	300	100
Kårvatn	Norway	NO0039R	Filter-3pack Filter-2pack	Daily	1980-2020	62.78333	8.88333	210	100
Tustervatn	Norway	NO0015R	Filter-3pack	Daily	1980-2020	65.83333	13.91667	439	100

			Filter-2pack						
Zeppelin Mountain	Norway	NO0042G	Filter-3pack	Daily	1990-2020	78.90715	11.88668	474	350
Leba	Poland	PL0004R	Filter-2pack Filter-1pack	Daily	1993-2020	54.75389	17.53426	2	100
Auchencorth Moss	Scotland	GB0048R	Online Ion Chroma.	Hourly	2007-2020	55.79216	-3.2429	260	250
Aspvreten	Sweden	SE0012R	Filter-3pack Filter-2pack Filter-1pack	Daily	1984-2017 (SO$_2$ from 1988)	58.8	17.38333	20	100

Table 1: Details of the 25 EMEP stations explored in this study which are shown geographically in Fig. 1. Stations highlighted in bold experienced at least one sulphurous pollution event between 1st September to 31st October 2014 attributed to Holuhraun emissions.

150

2.3 Numerical Model Simulations

Included in this study are Holuhraun eruption simulations by 5 GCMs: UKESM1, HadGEM3-GA7.0, MIROC6.1-SPRINTARS, ECHAM6.3-HAM2.3, and ECHAM6.3-HAM2.3-P3. Simulations are performed using the atmosphere-only component at a global scale (AMIP-style). To help clearly discriminate between signal and noise, the modelled horizontal
155   winds and potential temperature are constrained ("nudged") to ERA-Interim reanalysis data (Dee et al., 2011) on a 6-hourly time scale, and use monthly observational datasets to prescribe sea surface temperature and sea ice boundary conditions (e.g. HadISST, Rayner et al., 2003). All other modelled variables evolve physically and dynamically as their setup dictates and are subject to the parameterisations in play. Furthermore, the global 3-D CTM OsloCTM3 (Lund et al. 2018; Søvde et al., 2012) is included in this inter-model comparison. Unlike GCMs, CTMs do not simulate atmospheric dynamics explicitly, instead
160   OsloCTM3 uses pre-calculated 3-hourly meteorological fields from the European Centre for Medium-Range Weather Forecasts (ECMWF) forecast produced daily with a 12-hourly spin-up starting from ERA-Interim reanalysis. All numerical model simulations assume the eruption starts on 31st August 2014 and that the SO_2 emissions are distributed equally between 0.8 km and 3 km in the grid cell containing the eruption vent following the magnitude and altitude profile of emissions described in Malavelle et al. (2017). All models include additional background SO_2 emissions from anthropogenic and
165   natural sources. The simulations are continued from multiyear control simulations and are analysed at their native resolutions. Details specific to individual numerical models and key references can be found in Table 2.

8

Model Name	Modelling Centre	Chemistry/ Aerosol Module	Constraining/ Nudging Data	Spatial Resolution (Lat. x Lon.)	References
UKESM1	Met Office Hadley Centre, UK	UKCA-Mode	ERA-Interim	N96 L85 (1.25° x 1.875°)	Sellar et al., 2019 Dhomse et al., 2014
HadGEM3-GA7.0	Met Office Hadley Centre, UK	UKCA-Mode	ERA-Interim	N96 L85 (1.25° x 1.875°)	Williams et al., 2017 Dhomse et al., 2014
MIROC6.1-SPRINTARS	Research Institute for Applied Mechanics, Kyushu University, Japan	SPRINTARS	ERA-Interim	T213 L40 (0.5625° x 0.5625°)	Tatebe et al., 2019 Takemura et al., 2000, 2005, 2009
ECHAM6.3-HAM2.3	University of Oxford, UK	HAM (Default cloud microphysics scheme)	ERA-Interim	T63 L47 (1.875° x 1.875°)	Neubauer et al., 2019 Tegen et al., 2019 Stevens et al., 2013
ECHAM6.3-HAM2.3-P3	ETH Zurich, Zurich, Switzerland	HAM-P3 (P3 cloud microphysics scheme)	ERA-Interim	T63 L47 (1.875° x 1.875°)	Neubauer et al., 2019 Tegen et al., 2019 Dietlicher et al., 2018 Stevens et al., 2013
OsloCTM3	CICERO Center for International Climate Research, Norway	N/A	ECMWF Forecasts (Initiated with ERA-Interim)	N80 L60 (2.25° x 2.25°)	Lund et al., 2018 Søvde et al., 2012

Table 2: Details of the numerical models used in this study.

2.4 Backward Trajectories

The origin and age of air masses associated with sulphurous pollution events detected in the EMEP network observations are estimated using air parcel trajectories generated by the Hybrid Single Particle Lagrangian Integrated Trajectory (HYSPLIT) model developed by the National Ocean and Atmospheric Administration (NOAA) Air Resources Laboratory (Stein et al. 2015). For each EMEP station, a new 27-member ensemble of 10-day backward trajectories is initiated every hour at the altitudes listed in Table 1 from 1st September to 31st October 2014. Subsequently, events detected at stations sampling sulphur concentration daily have 25 ensembles (one for every hour including the bounding hours of the sampling) available to evaluate an event's origin and age, whilst stations sampling hourly will have 2 ensembles (the bounding hours of the sampling) to utilise. This equates to a total of 675 and 54 individual trajectories respectively. For consistency with the nudging of the models, ERA-Interim reanalysis data is used to run the HYSPLIT model which is applied at a regridded resolution of 1.0° x 1.0°. A limiting factor with using a backward trajectory analysis is that the trajectories are not expected to arrive exactly at the eruption vent and so a domain must be defined where trajectories within are deemed close enough to the volcano to be attributed. Defining this domain can be done visually through satellite imagery or by a statistical analysis, yet it is not trivial to generalise (Witham et al., 2021). Here we define this domain as a 3-D bounding box in the Holuhraun vicinity (20.33°W to 13.33°W, 63.35°N to 66.35°N, 0–4.5 km AMSL – see Fig. 1) and events with at least 2% of released trajectories passing through are attributed to volcanic emissions. The transport time of this subset of volcanically influenced events, essentially the age of the plume at the point of observation, are calculated using an averaging procedure. This procedure begins by considering only trajectories passing through the 3-D bounded domain (e.g. the red idealised trajectories in Fig 1.). For each of these trajectories, the age of the individual trajectory points residing in the bounding box (e.g. black circles in Fig 1.) are averaged resulting in the average transport time from the immediate Holuhraun vicinity to the EMEP station for a single trajectory. Finally, the transport time of the event, the plume age at the time of sampling, is calculated as the average of these individual single trajectory transport times (e.g. the average transport time of the two red idealised trajectories in Fig. 1).

Figure 1: Map of the 25 EMEP stations explored in this study. Stations marked with filled triangles experienced at least one sulphurous pollution event between 1st September to 31st October 2014 attributed to Holuhraun emissions. Stations marked with unfilled triangles either experienced no sulphurous pollution events or only events attributed to other sulphurous sources. A red star indicates the location of the Holuhraun eruption (64.85°N, 16.83°W) with the surrounding red dashed lines outlining the horizontal boundaries of the Holuhraun vicinity defined in this study (20.33°E to 13.33°W, 63.35°N to 66.35°N). Dotted lines show idealised backward trajectories initiated at Pallas Matorova for a single sulphurous pollution event with red and black lines representing trajectories that would and would not be attributed to the Holuhraun eruption respectively. Black circles represent idealised trajectory points that fall within the bounded Holuhraun vicinity.

11

3 SO₂ Plume Distribution, Height, and Mass Burden

13 Sep 2014 AM
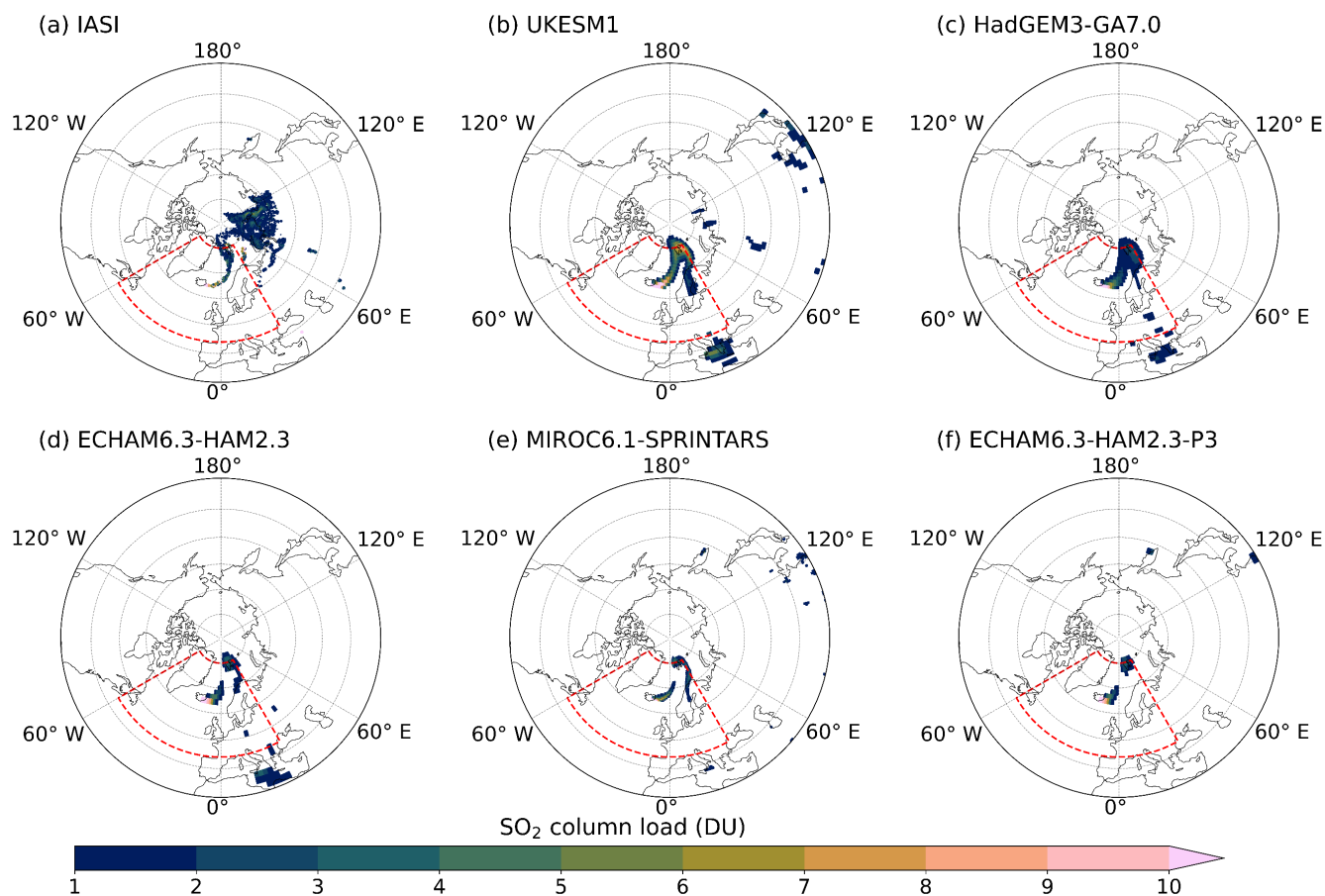
Figure 2: Comparison of volcanic SO₂ column load from (a) Infrared Atmospheric Sounding Interferometer (IASI) retrievals and (b, c, d, e, f) model simulations of the Holuhraun eruption on the morning of 13th September 2014. Red dashed area represents the Holuhraun region (44°N to 80°N, 60°W to 30°E) defined in this study. The model output is sampled at 09:00 UTC and 21:00 UTC for the AM and PM bidaily groups respectively Observed and simulated SO₂ column loads below 1 DU are masked to identify in-plume areas. IASI data and model output are shown on a 0.125° x 0.125° grid and at the resolutions given in Table 2 respectively. A full animation between 1st September to 31st October 2014 can be found in the Supplement (S1).

12

The bidaily SO_2 column load from the IASI retrievals and the model simulations between 1st September to 31st October 2014
215 feature in the animation in Supplement (S1) and the morning snapshot of the 13th September displayed in Fig. 2. The model
output is sampled at 09:00 UTC and 21:00 UTC for the AM and PM bidaily grouped retrievals respectively. Observed and
simulated SO_2 column loads below 1 DU are masked to identify in-plume areas as is done in other Holuhraun studies (e.g.
Haghighatnasab et al., 2022). This threshold is somewhat arbitrary yet strikes an acceptable balance in screening out enough
SO_2 from other sources within the red dashed Holuhraun region whilst not removing data associated with the main volcanic
220 plume. From Fig. 2 and the animation it is apparent that the Holuhraun eruption is observed and modelled as the main source
of SO_2 in the region, yet small areas of background SO_2 exist despite the plume detection screening (e.g. volcanic activity
from Mt. Etna). However, the contribution from these high background SO_2 sources relative to the total regional SO_2 is
minimal and unlikely to influence this study. Outside the Holuhraun region other SO_2 sources are more noticeable, such as
volcanic activity from the Kamchatka Peninsula and anthropogenic activity in Norilsk, Russia, yet their distances from the
225 area of interest mean they do not need to be considered further here. Both visualisations show that the models capture the
general features of the observed plume, particularly the dispersion over the Fennoscandian Peninsula and the UK during
September, suggesting that nudging the models to ERA-Interim reanalyses gives credence to the models' ability to accurately
simulate the plume dispersion despite their coarse resolution. The models often have larger plume areas, yet this is likely due
to IASI retrieval limitations (e.g. cloud cover, high latitude, swath width) rather than an overestimation. Despite
230 supplementing the MetOp-A IASI retrievals with that of MetOp-B, IASI coverage is limited during 17th–18th September and
9th–11th, 18th–19th, and 30th–31st October. Care should be taken when comparing IASI retrievals to the models across these
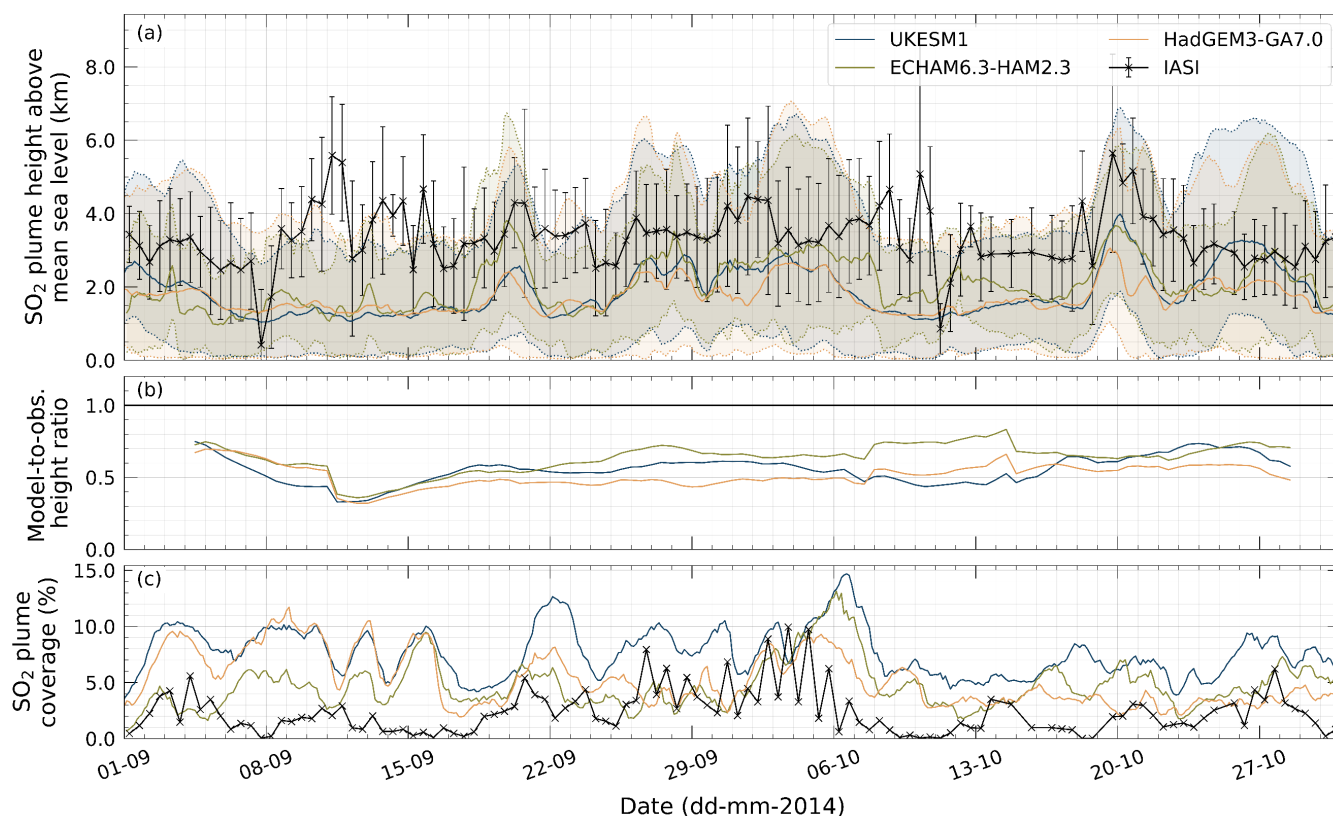dates.

Figure 3: (a) Instantaneous temporal evolution and (b) 7-day rolling mean of IASI retrieved and modelled plume SO_2 height across the Holuhraun region (44°N to 80°N, 60°W to 30°E) from 1st September to 31st October 2014. Black crosses and error bars represent the regional mean IASI SO_2 height and retrieval error. Modelled SO_2 heights are shown as a vertical profile. The solid-coloured lines represent the regional mean modelled central height of the SO_2 plume, and the associated envelope indicates the derived top and bottom regional mean heights of the SO_2 plume (see text). (c) The area the SO_2 plume covers as a percentage of the total Holuhraun region from 1st September to 31st October 2014.

The average observed and modelled SO_2 plume heights across the Holuhraun region from 1st September to 31st October are shown in Fig. 3a and are summarised in Table 3. The IASI retrievals show that the observed SO_2 plume height, specifically the central height of a Gaussian SO_2 vertical profile, exists primarily (~80%) between 2.5–4 km above mean sea level, very rarely exceeding 5 km, showing that the volcanic perturbation to the region is contained within the lower troposphere. On the morning of 1st September, the observed plume area (see animation in Supplement, S1) is centred close to the vent suggesting that the IASI retrieved height of 3.4 km is a good estimate for the plume injection height on this day. Fig. 3a shows the

14

modelled SO_2 plume vertical profiles across the Holuhraun region that are determined from the vertical cells within the in-plume areas with SO_2 mass concentrations exceeding 1 μgm^{-3}. The central height, given by a solid line, is the regional average of the mean cell height of those vertical cells above the threshold. The top and bottom heights, represented by the outer dotted lines enclosing the envelope, are the regional averages of the maximum and minimum cell heights of those vertical cells above the threshold. Generally, the models slightly underestimate the central plume height for most of September and October as shown in the 7-day rolling mean model-to-observed ratio in Fig. 3b. This underestimation is greatest during the second week of September when even the top heights of the modelled vertical profiles are below the observed peaks across 11th to 14th September. This feature may be a consequence of the vertical winds in the models not being constrained and/or additional variability in the momentum flux during the onset of the eruption which is not accounted for in the prescribed emission profile used in the models. From mid-September onwards the models' ability to capture the variability in plume height improves lying mostly within the estimated observational error. The bottoms of the modelled volcanic plumes are close to the surface suggesting that ground-based stations within the region are likely to experience moments of sulphurous pollution during September and October. Fig. 3c presents the in-plume area as a percentage of the Holuhraun region. The previous assessment that the modelled plumes occupy a greater area than the IASI plume is quantitively supported here. Fig. 3c shows that the sharp peaks and troughs in the observed plume height on 7th September and 10th, 11th, and 18th October occur during periods when the IASI coverage is very low and so may not reflect the height of the complete plume. The ECHAM6.3-HAM2.3-P3 simulation does not have the required output to estimate the SO_2 plume vertical profile at a bidaily resolution, yet the monthly mean central height shown in Table 3 of 1.8 km is close to the observed range which gives some confidence the model adequately captures the plume height within the Holuhraun region. Note that MIROC6.1-SPRINTARS simulation does not have the required output to estimate the SO_2 plume vertical profile.

The IASI retrieved and modelled SO_2 mass burdens across the Holuhraun region from 1st September to 31st October are summarised in Table 3 with the time series provided in the Supplement (S2). The SO_2 mass burdens are obtained by summing the product of the individual in-plume pixel/grid cell SO_2 column load and corresponding surface area across the region for each time step. The same method is applied to the SO_2 column load IASI retrieval error to estimate an SO_2 mass burden observational error. Across September and October, the average bidaily SO_2 mass burden from IASI is 63 ± 23 kt of SO_2, yet there is substantial variation evident by the peaks of 204 ± 61 kt of SO_2, 179 ± 55 kt of SO_2 and 163 ± 47 kt of SO_2 on 5th, 20th and 23rd September respectively, and the low values below 10 kt of SO_2 (e.g. 7th and 13th September, 10th and 18th October). This variation is likely caused by a combination of the plume passing in and out of the defined region and changing IASI retrieval coverage (see Fig. 3c) as opposed to physical or chemical processes, such as substantial fluctuations in the volcanic SO_2 emission flux. The models simulate an average bidaily SO_2 mass burden in agreement with that derived from the satellite instrumentation, aside from UKESM1 and MIROC6.1-SPRINTARS that respectively overestimate and underestimate the IASI derived totals. As the IASI instrumentation is not able to sample the full intricacies of the plume, the SO_2 mass burden presented here is to be considered as a lower estimate and so UKESM1 exceeding this may not necessarily

15

be an indicator of poor performance. All models simulate a maximum SO_2 mass burden in September when the eruption is

285   most powerful and prescribed emission rates the highest, before decreasing during October illustrating that they capture the

observed variability well. Interestingly, there is a noticeable range in the general magnitude of the simulated mass burdens

despite each model using the same prescribed emission profile. Correcting the IASI retrievals for parts of the SO_2 plume

potentially missing has proved valuable (e.g. Carboni et al., 2019a) and could improve the agreement with the modelled

heights and mass burdens, yet as the general variability of both is well captured and no significant defects exist, using a

290   cloud-adjusted correction is deemed unnecessary here. Note the OsloCTM3 simulation does not have the required

diagnostics to compare the SO_2 plume evolution with IASI retrievals.

		IASI	UKESM1	HadGEM3-GA7.0	MIROC6.1-SPRINTARS	ECHAM6.3-HAM2.3-P3	ECHAM6.3-HAM2.3	OsloCTM3
SO₂ Plume Altitude (km)	Max.	5.6 ± 2.7	4.0	3.1	-	-	3.8	-
	Min.	0.4 ± 1.5	1.0	1.2	-	-	1.0	-
	Mean	3.4 ± 1.4	1.9	1.7	-	1.8	2.1	-
SO₂ Mass Burden (kt of SO₂)	Max.	204 ± 61	393	225	109	128	176	-
	Min.	0.10 ± 0.04	69	29	7	9	18	-
	Mean	63 ± 23	171	86	35	55	76	-

Table 3: IASI retrieved and simulated SO_2 plume altitude and SO_2 mass burden across the Holuhraun region (44°N to 80°N,

295   60°W to 30°E) from 1st September to 31st October 2014.
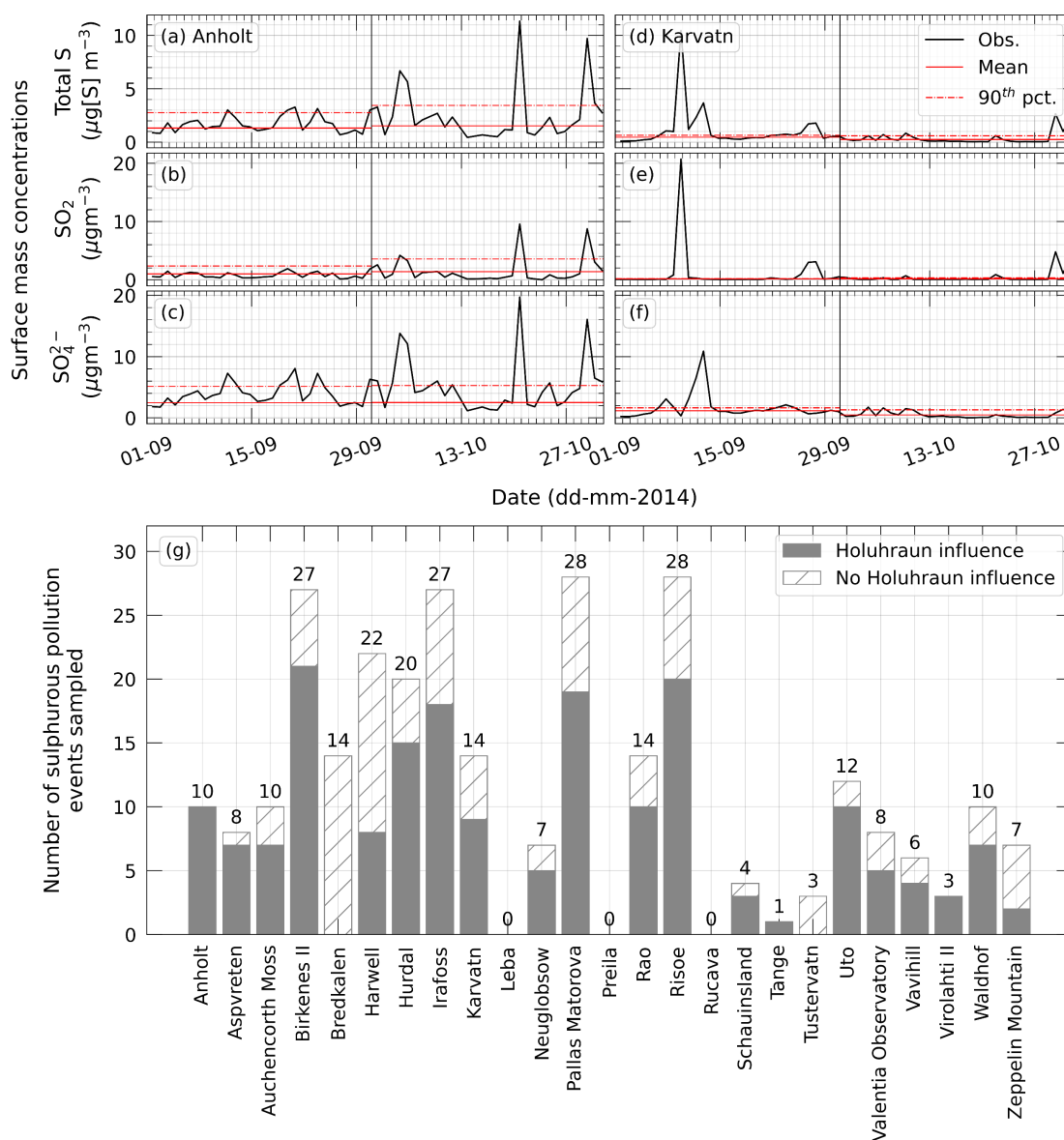
4 Sulphurous Surface Mass Concentrations

Figure 4: Observed surface mass concentration time series of total sulphur content, SO_2 and SO_4^{2-} at (a, b, c) Anholt (Denmark) and (d, e, f) Kårvatn (Norway) between 1st September and 31st October 2014. Climatological monthly mean and 90th percentile values are given in the red solid and dashed lines respectively. (g) Number of sulphurous pollution events identified across the 25 EMEP stations categorised in terms of those attributed to Holuhraun emissions (solid fill) and those attributed to other sulphurous sources (hash fill).

Observed time series of surface mass concentrations of total sulphur content, SO_2 and SO_4^{2-} from 1st September to 31st
305   October at EMEP stations Anholt (Denmark) and Kårvatn (Norway) are shown in Fig. 4a-c and Fig. 4d-f respectively. Time
series of the other 23 EMEP stations are provided in the Supplement (S3-25). Anholt and Kårvatn feature numerous peaks in
sulphurous concentrations that exceed the climatological monthly statistics suggesting that these are significant and, given
their rural locations, are likely caused by far afield sources of pollutants. Using the definition given in Sect. 2.2, we find that
Anholt experienced 10 pollution events during September and October whilst Kårvatn experienced 14. We see merit in
310   defining a pollution event using the total sulphur content concentration, rather than the commonly used SO_2 concentration
(e.g. Boichu et al., 2019), as additional events are identified due to their high SO_4^{2-} concentrations which otherwise would
have been missed (e.g. Anholt on 19th, 20th and 23rd September, Kårvatn on 11th and 12th September). Fig. 4g displays the
number of sulphurous pollution events observed across the selected 25 EMEP stations during September and October.
Birkenes II (Norway), Irafoss (Iceland), Pallas Matorova (Finland) and Risoe (Denmark) all experienced roughly an event
315   every two days, whilst only Leba (Poland), Preila (Lithuania) and Rucava (Latvia) did not experience any. In total, 283
pollution events are observed across Europe at 22 EMEP stations indicating that widespread sulphurous pollution occurred in
the months following the eruption.

The likelihood of Holuhraun being a main source of pollution for the 283 events can be established qualitatively using the
320   IASI retrieved and modelled SO_2 column load animations in the Supplement (S1) or more robustly using a trajectory
analysis as described in Sect. 2.4. Using the latter approach, the main source of pollution for 184 (65%) of the events can be
attributed to Holuhraun emissions (see Fig. 4g for a station-by-station breakdown). Of the 22 EMEP stations experiencing a
pollution event between September and October 2014, 20 endured at least one influenced by the eruption. Note that other
sources of pollutants may also contribute to these 184 events, yet these contributions are likely minor given that Holuhraun is
325   the predominate sulphurous source in the region covering this period. None of the combined 17 events observed at
Bredkälen (Sweden) and Tustervatn (Norway) are attributed to Holuhraun emissions which, given that the plume has been
shown to pass this area (e.g. Grahn et al., 2015; Ialongo et al., 2015), suggests an inconsistency in the trajectory analysis. The
choice of the input meteorological dataset is shown to dominate the uncertainty in trajectory calculations with the choice of
trajectory model playing a smaller role, although no combination of the two is found superior (Gebhart et al., 2005) and so
330   changing them is unlikely to improve the analysis here. Instead, the inconsistency could be resolved by amending the
initialisation altitudes of the two stations. Nevertheless, the trajectory analysis shows that Holuhraun brought about
significantly elevated sulphurous surface mass concentrations across Europe which is testament to the sheer volume of SO_2
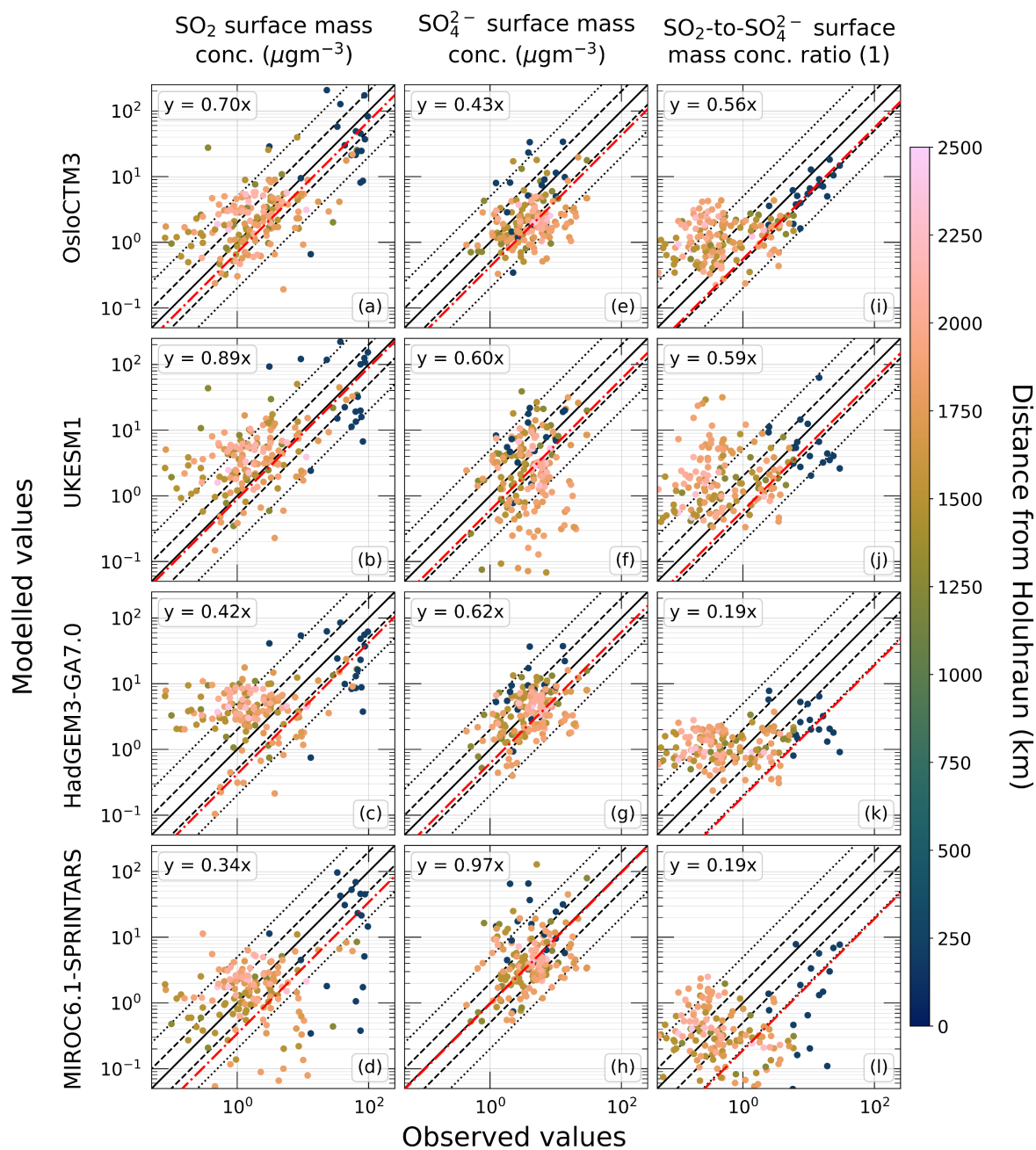emitted into the region by the eruption.

Figure 5: Modelled versus observed surface mass concentrations of SO_2 and SO_4^{2-}, and the SO_2-to-SO_4^{2-} ratio for 184 sulphurous pollution events attributed to Holuhraun emissions across 22 EMEP stations from 1st September to 31st October 2014. Black lines from the inside out represent the 1:1, 2:1 and 5:1 boundaries, whilst the red dashed lines represent the linear regression fit. Note that observational errors are too small to be discernible.

340

Our catalogue of volcanically influenced events is used to assess model performance in capturing the surface level behaviour of the plume. Fig. 5 shows the modelled versus observed surface mass concentrations of SO_2 (a, b, c, d) and SO_4^{2-} (e, f, g, h), and the SO_2-to-SO_4^{2-} ratio (i, j, k, l) of the 184 volcanic events for OsloCTM3, UKESM1, HadGEM3-GA7.0 and MIROC6.1-SPRINTARS. The remaining models are found in the Supplement (S26). The performance of the models is summarised in

345 Table 4. The ability of the models to capture the observed SO_2 concentrations varies. Whilst OsloCTM3 and UKESM1 perform best with regression lines close to parity and 83.7% and 71.7% of values within the 5:1 range respectively, the remaining models struggle, most notably the ECHAM6.3 configurations with both having less than 58% of values within the 5:1 range. Observed SO_2 concentrations decrease with increasing distance from the eruption. Aside from ECHAM6.3-HAM2.3-P3, the models tend to overestimate the observed SO_2 surface mass concentrations at stations distanced greater than

350 1300 km from Holuhraun. Interestingly, Schmidt et al. (2015) found that NAME simulations underestimate the observed SO_2 surface mass concentrations at four Irish air quality monitoring stations each distanced between 1400 km and 1450 km away from the eruption. However, neither the NAME model or those stations are explored in this study and so a direct comparison is not possible. In addition, all models tend to underestimate the higher SO_2 concentrations observed at stations closer to Holuhraun which, coupled with the SO_2 overestimation at stations further away, could suggest that the removal of

355 tropospheric SO_2 in the models is too slow in the region following the eruption.

20

		UKESM1	HadGEM3-GA7.0	MIROC6.1-SPRINTARS	ECHAM6.3-HAM2.3-P3	ECHAM6.3-HAM2.3	OsloCTM3
Regression Coefficient	SO_2	0.89 ± 0.08	0.42 ± 0.04	0.34 ± 0.03	0.118 ± 0.009	0.16 ± 0.02	0.70 ± 0.07
	SO_4^{2-}	0.60 ± 0.06	0.62 ± 0.05	0.97 ± 0.13	0.82 ± 0.08	1.32 ± 0.11	0.43 ± 0.05
	SO_2-to-SO_4^{2-} Ratio	0.60 ± 0.11	0.19 ± 0.02	0.19 ± 0.02	0.091 ± 0.013	0.08 ± 0.02	0.56 ± 0.03
Values within 5:1	SO_2	132 (71.7%)	121 (65.8%)	129 (70.1%)	91 (49.5%)	105 (57.1%)	154 (83.7%)
	SO_4^{2-}	144 (78.3%)	173 (94.0%)	157 (85.3%)	158 (85.9%)	156 (84.8%)	152 (82.6%)
	SO_2-to-SO_4^{2-} Ratio	96 (52.2%)	109 (59.2%)	100 (54.3%)	101 (54.9%)	114 (62.0%)	121 (65.8%)

Table 4: Summary of the modelled versus observed surface mass concentration behaviour of the 184 sulphurous pollution events attributed to Holuhraun emissions.
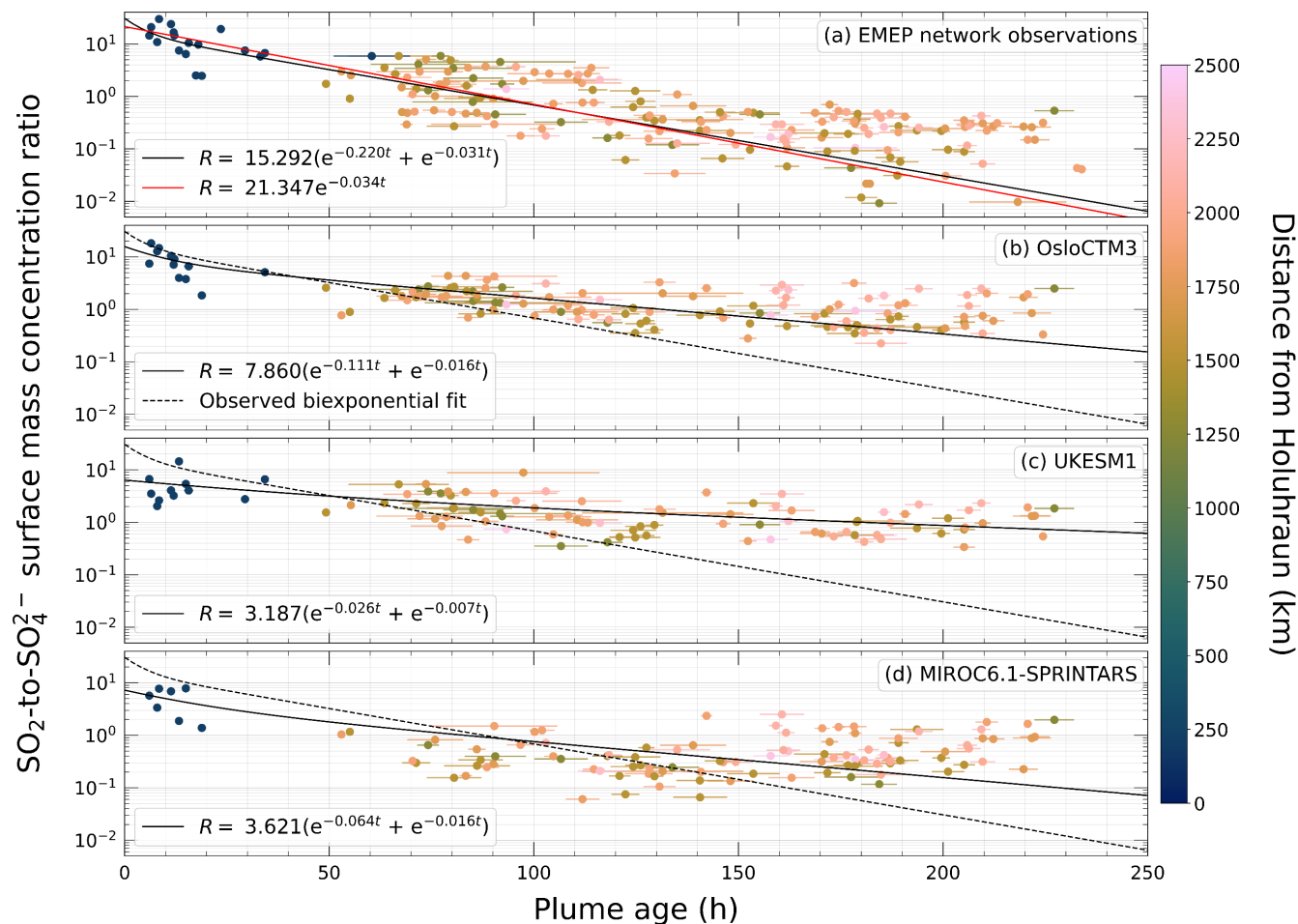
The observed SO_4^{2-} surface mass concentrations displayed in Fig. 5e-h show no clear correlation with distance from the eruption vent. Relative to their SO_2 regression lines, OsloCTM3 and UKESM1 perform poorer in replicating SO_4^{2-} surface mass concentrations whilst the remaining model performances improve, particularly MIROC6.1-SPRINTARS with a slope of 0.97 ± 0.13 and HadGEM3-GA7.0 where 94.0% of modelled concentrations lie within the 5:1 range. There is no apparent overestimation or underestimation of SO_4^{2-} concentrations across the models, aside from perhaps in UKESM1 where underestimation occurs at some stations distanced greater than 1700 km from Holuhraun. The models struggle most in capturing the SO_2-to-SO_4^{2-} ratio shown in Fig. 5i-l as only UKESM1 and OsloCTM3 show modelled regression slopes above 0.55. Although this poor performance relative to the simulation of the individual SO_2 and SO_4^{2-} concentrations is somewhat expected as the models are essentially trying to correctly capture the behaviour of two pollutants as opposed to one. Observed and modelled ratios become smaller with increasing distance from the volcanic vent suggesting that SO_2 oxidation to SO_4^{2-} is occurring within the observed and simulated plumes. Possible causes of differences between observed and

simulated surface level behaviour of far afield Holuhraun pollutants, such as vertical resolution, source emission profile, and

375   sub grid turbulence parameterisations, have been explored in depth previously (e.g. Boichu et al., 2016; Schmidt et al.,

2015). These challenges are not specific to Holuhraun and feature extensively in most numerical dispersion problems and so

should not act as evidence that a model is not fit to be used in Part 2 of this study. In fact, given the relatively fine spatial and

temporal resolution that these coarse models are being assessed against, they perform commendably in capturing the surface

level behaviour of the plume.

5 Rate of In-Plume SO_2 oxidation to SO_4^{2-}

The pathways of SO_2 oxidation to SO_4^{2-} are essentially through gas-phase (slower) and aqueous-phase (faster) reactions with

the hydroxyl radical (OH^-) and hydrogen peroxide (H_2O_2) respectively (e.g. Calvert et al., 1978). The ratio of SO_2-to-SO_4^{2-} is

therefore useful in assessing whether oxidation processes are accurately represented in models; a ratio greater than that

observed suggests that one or both oxidation processes are too slow whilst a ratio less than that observed suggests that one or

385   both oxidation processes are too fast. By using the ratio of the two pollutants, the variation in the absolute Holuhraun daily

sulphurous emission flux can be ignored. Here the SO_2 oxidation to SO_4^{2-} is explored using our catalogue of pollution events

attributed to Holuhraun emissions across the 22 EMEP stations. For each event, the trajectory analysis used previously to

verify volcanic influence is now used to estimate the transport time of the plume to the station, essentially the plume age,

following the method outlined in Sect. 2.4.

Figure 6: (a) Observed and (b-d) modelled SO_2-to-SO_4^{2-} surface mass concentration ratios of sulphurous pollution events attributed to Holuhraun emissions with respect to the plume age (see Sect. 2.4). Red and black solid lines represent monoexponential and biexponential fits respectively. Black dashed lines represent the observed biexponential fit overlayed on the model simulation subplots. Note the observed ratio errors are too small to be discernible.

Fig. 6a shows the observed surface mass concentration ratio of SO_2-to-SO_4^{2-} for the 184 events versus the age of the plume at the time of sampling (Sect. 2.4). A variety of plume ages are estimated ranging from 6 h to 234 h with the plume associated with events observed at stations closer to Holuhraun generally being younger than events observed further away. Such a considerable difference in the estimated parcel age, coupled with a large range in observed ratios (0.01 to 29.75) likely means that the local volcanic pollution sampled across the 22 EMEP stations stems from the plume during different stages of its lifetime. It is worth noting that even some individual stations experience the plume at notably varying ages such as Utö (Finland) where events are associated with the plume aged between 96 h to 210 h. Similarly, the observed SO_2-to-SO_4^{2-} ratio

varies up to an order of magnitude for the plume at comparable ages. This variability is visible in the apparent vertical spread
of the data in Fig. 6a. For example, plume ages between 70 h to 80 h have SO_2-to-SO_4^{2-} ratios between 0.5 and 5.9. Both
these variations noted at individual stations and within the plume at similar ages is testament to the complexity of SO_2
oxidation to SO_4^{2-} within volcanic plumes and may be related to the relative contribution of the gas-phase and aqueous-phase
pathways, although oxidant limitation (i.e. the SO_2 concentrations may be so high that OH^- and/or H_2O_2 are reduced to such
an extent that the reactions cease to occur) may also play a key role as it has been shown for the Kīlauea volcano, Hawaii
(Pattantyus et al., 2018).

The linear characteristics of Fig. 6a hint at an observed exponential decay between the SO_2-to-SO_4^{2-} ratio and plume age.
This relationship is clearer in the equivalent linear scale figure contained in the Supplement (S28). The observed data is
fitted to monoexponential and biexponential functions. A biexponential function, a sum of two individual exponential decay
components, is chosen to assess the feasibility in distinguishing between the decay caused by gas-phase and aqueous-phase
oxidation. Both functions are fitted using non-linear total least squares regression which considers both the ratio and plume
age uncertainties. The biexponential function better captures the observations and so will be the focus here. The observed
biexponential decay components suggest a gas-phase SO_2 oxidation rate of 0.031 ± 0.002 h^{-1} and an aqueous-phase SO_2
oxidation rate of 0.22 ± 0.16 h^{-1} corresponding to e-folding times of 1.34 ± 0.07 days and 0.19 ± 0.14 days respectively.
Using IASI retrieved SO_2 column loads, Carboni et al. (2019) estimate Holuhraun having a mean 6-month SO_2 e-folding
time of 2.4 ± 0.6 days whilst Schmidt et al. (2015) derive a mean September SO_2 e-folding time of 2.0 ± 0.8 days using
NAME simulations of the eruption. Whilst not directly comparable, as these studies have not treated the two oxidation
pathways individually and focus on different time periods, both estimates are consistent with the gas-phase SO_2 e-folding
time found here. Assuming the biexponential decay relationship holds close to the eruption vent, this study estimates a near-
vent ratio of 31 ± 4. This result agrees with Ilyinskaya et al. (2017) where SO_2-to-SO_4^{2-} ratios of 2 to 250 and 4 to 94 are
observed at 100 km and 250 km from the vent respectively. Boichu et al. (2019) estimate a lower near-vent ratio of 19.7
using a similar method presented here, yet this study assumes the ratio evolves linearly and considers only 5 events with
plume ages ranging from 50 h to 80 h.

Fig. 6b-d shows the modelled surface mass concentration ratio of SO_2-to-SO_4^{2-} versus the age of the plume these ratios are
simulated in for OsloCTM3, UKESM1 and MIROC6.1-SPRINTARS. The remaining models are found in the Supplement
(S27-28). All models display an exponential relationship between the SO_2-to-SO_4^{2-} and plume age. Each model is fitted to a
biexponential function which is given by the solid line with the observed fit overlayed in the dashed line for comparison. Of
the 184 surface level pollution events attributed to Holuhraun emissions, only those deemed to have been successfully
captured by a model are used for each fit. A modelled event is considered successful if both the surface mass concentrations
of SO_2 and SO_4^{2-} are within a 5:1 range of that observed. There is no requirement on the value of the modelled SO_2-to-SO_4^{2-}
ratio. The number of successfully modelled events and the biexponential parameter estimates for all models are displayed in

Table 5. The modelled near-vent ratios are all smaller than that derived from observations, yet all agree with those found by
Ilyinskaya et al. (2017). All model derived gas-phase oxidation rates are slower than that derived from observations ranging
440 from roughly being twice as slow in OsloCTM3 and MIROC6.1-SPRINTARS, to up to 10 times as slow in HadGEM3-
GA7.0. Better agreement is found with the derived aqueous-phase oxidation rates with OsloCTM3, MIROC6.1-SPRINTARS
and HadGEM3-GA7.0 in agreement with the observation derived value. However, the derived aqueous-phase oxidation rate
in UKESM1 and ECHAM6.3-HAM2.3-P3 are slower than observed. Note that ECHAM6.3-HAM2.3 cannot be described
sufficiently by a biexponential function and so the oxidation rate and *e*-folding time here relate to the overall oxidation and
445 are derived from a monoexponential function (i.e. one decay component only) preventing a direct comparison with the
derived observed values.

	Observations	UKESM1	HadGEM3-GA7.0	MIROC6.1-SPRINTARS	ECHAM6.3-HAM2.3-P3	ECHAM6.3-HAM2.3*	OsloCTM3
Events (Successfully Modelled)	184 (-)	99 (53.8%)	115 (62.5%)	108 (58.7%)	86 (46.7%)	89 (48.4%)	130 (70.7%)
Near-Vent SO_2-to-SO_4^{2-} Ratio	31 ± 4	6.4 ± 0.7	3.9 ± 0.6	7.2 ± 1.4	2.7 ± 0.3	2.2 ± 0.4	16 ± 3
Aqueous Oxidation Rate (h^{-1})	0.22 ± 0.16	0.03 ± 0.02	0.04 ± 0.03	0.06 ± 0.07	0.02 ± 0.02	0.010 ± 0.002	0.11 ± 0.09
Aqueous *e*-folding Time (days)	0.19 ± 0.14	1.6 ± 1.0	1.1 ± 1.0	0.7 ± 0.7	2 ± 2	4.2 ± 0.8	0.4 ± 0.3
Gaseous Oxidation Rate (h^{-1})	0.031 ± 0.002	0.007 ± 0.002	0.003 ± 0.001	0.016 ± 0.002	0.007 ± 0.002	-	0.016 ± 0.003
Gaseous *e*-folding Time (days)	1.34 ± 0.07	6.3 ± 1.4	13 ± 5	2.6 ± 0.4	6 ± 2	-	2.7 ± 0.4

Table 5: Summary of the observed and modelled in-plume SO_2 oxidation to SO_4^{2-} using the sulphurous pollution events
450 attributed to Holuhraun emissions. Note that ECHAM6.3-HAM2.3 cannot be described sufficiently by a biexponential
function and so the oxidation rate and *e*-folding time here relate to the overall oxidation and are derived from a
monoexponential function (i.e. one decay component only).

25

5 Summary and Conclusions

By releasing 9.6–11.8 Mt of SO_2 into the lower troposphere across nearly 6 months, the 2014–2015 Holuhraun eruption
455 offers an opportunity to challenge the capability of GCMs in capturing the characteristics of tropospheric sulphate aerosol
intricacies resulting from effusive eruptions and assess the potential impact of subsequent aerosol-cloud interactions. A
model inter-comparison effort has been initiated to leverage this opportunity and the results from Part 1 of the two-part
analysis are presented here. Remote sensing data of SO_2, and surface level SO_2 and SO_4^{2-} mass concentration measurements
are used in conjunction with trajectory modelling to evaluate the performance of 5 GCMs and a CTM in simulating the
460 spatial and chemical evolution of the SO_2 plume across the North Atlantic and Europe.

A comparison against IASI SO_2 retrievals show that the models capture the evolution of the volcanic plume within the
surrounding region well during September and October 2014. Holuhraun emissions are the dominant source of SO_2 in the
models and the spatial transport of the associated SO_2 plume is well replicated. The vertical distribution of the SO_2 plume is
465 slightly underestimated by the models, whereas there is no general overestimation or underestimation in simulating the SO_2
mass burdens; it is model dependent. The temporal variability of both plume characteristics is well captured. Discrepancies
with the IASI retrievals could be due to several factors including the limitations of the IASI retrievals (e.g. Carboni et al.,
2019a), and discrepancies between the idealised volcanic emission profile used by the models and the real emissions (e.g.
Steensen et al., 2016). A comparison against retrievals of volcanic SO_2 from other satellite instrumentations may yield
470 different conclusions, yet the descriptions of the plume spatial distribution made with other remote sensing products are
similar (e.g. OMI: Ialongo et al., 2015; Schmidt et al., 2015, Steensen et al., 2016; OMPS-NN: Ialongo et al., 2015; GOME-
2: Twigg et al., 2016). Even though model representations of the eruption are not perfect, the intent here is rather to assess
the SO_4^{2-} production in the different models whilst considering everything else equal (i.e. same emissions) as understanding
the aerosol perturbation will help discern the impact on cloud properties and assess the ACIs in Part 2.

475

By combining the surface mass concentration measurements of SO_2 and SO_4^{2-} made during September and October 2014
across the EMEP network with trajectories calculated using the HYSPLIT model, the simulated surface level behaviour of
the plume was assessed. Of the 283 sulphurous pollution events identified, 184 are attributed to Holuhraun emissions.
Generally, the models reproduce the measured elevated surface level concentrations during these volcanically influenced
480 events, yet they struggle in simulating the correct magnitude, notably SO_2 which is often overestimated. Although, as noted
in Boichu et al. (2016), capturing volcanic sulphurous pollutant surface mass concentrations far afield at a specific location
and time is challenging even for CTMs with fine resolutions. Given the relatively coarse scale of the simulations discussed
here, the surface level performance of the models is admirable.

485 Both the observed and modelled ratios of SO_2-to-SO_4^{2-} surface mass concentration sampled within the plume are shown to
decrease with increasing station distance from the eruption vent suggesting SO_2 oxidation to SO_4^{2-} is occurring. To explore

26

this further, the ratios as a function of plume age have been analysed revealing an exponential decay. By fitting this decay to a biexponential function, the gas-phase and aqueous-phase oxidation pathways can be estimated with their rates represented by the biexponential decay components. All models aside from ECHAM6.3-HAM2.3 benefit from the use of a biexponential

490 fit to describe the SO_2 decay suggesting that they replicate two oxidation pathways within the plume. The modelled derived aqueous-phase oxidation rates are in better agreement than the gas-phase oxidation rates with the observation derived values, yet altogether the oxidation in the modelled plumes are found to occur too slowly. This indicates that the volcanic SO_2 introduced into the simulations may not be chemically converted fast enough relative to what is derived from surface measurements. This study acknowledges that substantial assumptions are required to draw these conclusions, such as

495 ignoring the effect of deposition.

Overall, the 6 models considered here provide reasonable simulations of the spatial and chemical evolution of the Holuhraun plume and are considered competent enough to be used to explore the impacts of the eruption on ACIs (see Part 2 of this study). It is important to acknowledge, and is possibly relevant to the wider ACI community, that this analysis has also

500 highlighted that the models do not perfectly capture the secondary SO_4^{2-} aerosol production during a large degassing event which may contribute to disagreements between model ACIs estimates due to differing underlying perturbations. We hope that our application of in situ sulphurous surface measurements to assess numerical models help bolster the case to retain and extend air monitoring networks of volcanic pollutants for use in future studies.

Code Availability

505 Code is available from the corresponding author on reasonable request.

Data Availability

The IASI SO_2 retrieval dataset is available on the CEDA Archive, https://catalogue.ceda.ac.uk/uuid/d40bf62899014582a72d24154a94d8e2 (Carboni et al., 2019b). The EMEP network surface SO_2 and SO_4^{2-} mass concentrations are available through the EBAS database, https://ebas.nilu.no/data-access/. All model

510 data, including trajectory output, used in this study is available on Zenodo, https://doi.org/10.5281/zenodo.7786775 (Jordan, 2023).

Author Contributions

GJ, JH and FM designed the experiment. GJ handled the remote sensing data and in situ surface measurements whilst GJ, DW-P, TT, DN, GM and RS ran the model simulations. PK and DGP provided HYSPLIT trajectories and offered guidance in

their use. GJ, JH, FM, YC, AP, ED and DGP analysed the spatial and chemical evolution of the Holuhraun plume. GJ prepared the manuscript with contributions from all co-authors.

Competing Interest

At least one of the (co-)authors is a member of the editorial board of Atmospheric Chemistry and Physics. The peer-review process was guided by an independent editor, and the authors also have no other competing interests to declare.

Acknowledgements

References

Aas, W., Mortier, A., Bowersox, V., Cherian, R., Faluvegi, G., Fagerli, H., Hand, J., Klimont, Z., Galy-Lacaux, C., Lehmann, C. and Myhre, C.L.: Global and regional trends of atmospheric sulfur. Scientific reports, 9, 953, doi:10.1038/s41598-018-37304-0, 2019.

Ágústsdóttir, T., Woods, J., Greenfield, T., Green, R. G., White, R. S., Winder, T., Brandsdóttir, B., Steinthórsson, S., and Soosalu, H.: Strike-slip faulting during the 2014 Bárðarbunga-Holuhraun dike intrusion, central Iceland, Geophys. Res. Lett., 43, 1495– 1503, doi:10.1002/2015GL067423, 2016.

Arason, Þ., Bjornsson, H., Petersen, G. N., Jónasdóttir, E. B., and Oddsson B. B.: Plume height during the 2014–2015 Holuhraun volcanic eruption, Geophys. Res., Abstracts, EGU2015-11498, 2015.

Athanassiadou, M., Francis, P. N., Saunders, R. W., Atkinson, N. C., Hort, M. C., Havemann, S., Thelen, J.-C. and Bush, M.: A case study of sulphur dioxide identification in three different volcanic eruptions, using Infrared satellite observations (IASI), Met. Apps., 23, 477-490, doi: 10.1002/met.1572, 2016.

Barsotti, S.: Probabilistic hazard maps for operational use: the case of SO$_2$ air pollution during the Holuhraun eruption (Bárðarbunga, Iceland) in 2014–2015, Bull. Volcanol., 82, 56, doi:10.1007/s00445-020-01395-3, 2020.

Barsotti, S., Oddsson, B., Gudmundssonc, M. T., Pfeffer, M. A., Parks, M. M., Ófeigsson, B. G., Sigmundsson, F., Reynisson, V., Jónsdóttir, K., Roberts, M. J., Heiðarsson, E. P., Jónasdóttir, E. B., Einarsson, P., Jóhannsson, T., Gylfason, Á. G., and Vogfjörd, K.: Operational response and hazards assessment during the 2014–2015 volcanic crisis at Bárðarbunga volcano and associated eruption at Holuhraun, Iceland, J. Volcanol. Geotherm., 390, 106753, doi:10.1016/j.jvolgeores.2019.106753, 2020.

Boichu, M., Chiapello, I., Brogniez, C., Péré, J.-C., Thieuleux, F., Torres, B., Blarel, L., Mortier, A., Podvin, T., Goloub, P., Söhne, N., Clarisse, L., Bauduin, S., Hendrick, F., Theys, N., Van Roozendael, M., and Tanré, D.: Current challenges in modelling far-range air pollution induced by the 2014–2015 Bárðarbunga fissure eruption (Iceland), Atmos. Chem. Phys., 16, 10831–10845, doi:10.5194/acp-16-10831-2016, 2016.

550   Boichu, M., Favez, O., Riffault, V., Petit, J.-E., Zhang, Y., Brogniez, C., Sciare, J., Chiapello, I., Clarisse, L., Zhang, S., Pujol-Söhne, N., Tison, E., Delbarre, H., and Goloub, P.: Large-scale particulate air pollution and chemical fingerprint of volcanic sulfate aerosols from the 2014–2015 Holuhraun flood lava eruption of Bárðarbunga volcano (Iceland), Atmos. Chem. Phys., 19, 14253–14287, doi:10.5194/acp-19-14253-2019, 2019.

Breen, K. H., Barahona, D., Yuan, T., Bian, H., and James, S. C.: Effect of volcanic emissions on clouds during the 2008 and 555   2018 Kilauea degassing events, Atmos. Chem. Phys., 21, 7749–7771, doi:10.5194/acp-21-7749-2021, 2021.

Calvert, J.G., Bottenheim, J.W. and Strausz, O.P.: Mechanism of the homogeneous oxidation of sulfur dioxide in the troposphere, Atmos. Environ., 12, 197-226, doi:10.1016/0004-6981(78)90201-9, 1978.

Carboni, E., Grainger, R., Walker, J., Dudhia, A., and Siddans, R.: A new scheme for sulphur dioxide retrieval from IASI measurements: application to the Eyjafjallajökull eruption of April and May 2010, Atmos. Chem. Phys., 12, 11417–11434, 560   doi:10.5194/acp-12-11417-2012, 2012.

Carboni, E., Grainger, R. G., Mather, T. A., Pyle, D. M., Thomas, G. E., Siddans, R., Smith, A. J. A., Dudhia, A., Koukouli, M. E., and Balis, D.: The vertical distribution of volcanic SO_2 plumes measured by IASI, Atmos. Chem. Phys., 16, 4343–4367, doi:10.5194/acp-16-4343-2016, 2016.

Carboni, E., Mather, T. A., Schmidt, A., Grainger, R. G., Pfeffer, M. A., Ialongo, I., and Theys, N.: Satellite-derived sulfur 565   dioxide (SO2) emissions from the 2014–2015 Holuhraun eruption (Iceland), Atmos. Chem. Phys., 19, 4851–4862, doi:10.5194/acp-19-4851-2019, 2019a.

Carboni, E., Taylor, I., and Grainger, D.: IASI retrieval of sulphur dioxide (SO_2) column amounts and altitude, 2014-09 to 2015-02, version 1.0. Centre for Environmental Data Analysis, https://catalogue.ceda.ac.uk/uuid/d40bf62899014582a72d24154a94d8e2, 2019b.

570   Carn, S. A., Yang, K., Prata, A. J., and Krotkov, N. A.: Extending the long-term record of volcanic SO_2 emissions with the Ozone Mapping and Profiler Suite nadir mapper, Geophys. Res. Lett., 42, 925– 932, doi:10.1002/2014GL062437, 2015.

Chen, Y., Haywood, J., Wang, Y., Malavelle, F., Jordan, G., Partridge, D., Fieldsend, J., De Leeuw, J., Schmidt, A., Cho, N., Oreopoulos, L., Platnick, S., Grosvenor, D., Field, P., and Lohmann, U.: Machine learning reveals climate forcing from aerosols is dominated by increased cloud cover, Nat. Geosci., 15, 609–614, doi:10.1038/s41561-022-00991-6, 2022.

575   Clarisse, L., Coheur, P. F., Prata, A. J., Hurtmans, D., Razavi, A., Phulpin, T., Hadji-Lazaro, J., and Clerbaux, C.: Tracking and quantifying volcanic SO_2 with IASI, the September 2007 eruption at Jebel at Tair, Atmos. Chem. Phys., 8, 7723–7734, doi:10.5194/acp-8-7723-2008, 2008

Clarisse, L., Hurtmans, D., Prata, A. J., Karagulian, F., Clerbaux, C., De Mazière, M., Coheur, P. F.: Retrieving radius, concentration, optical depth, and mass of different types of aerosols from high-resolution infrared nadir spectra, Appl. Opt., 580   49, 3713-3722, doi:10.1364/AO.49.003713, 2010.

Crameri, F.: Scientific colour maps, Zenodo, http://doi.org/10.5281/zenodo.1243862, 2018.

Dee, D. P., Uppala, S. M., Simmons, A. J., Berrisford, P., Poli, P., Kobayashi, S., Andrae, U., Balmaseda, M. A., Balsamo, G., Bauer, P., Bechtold, P., Beljaars, A. C. M., van de Berg, L., Bidlot, J., Bormann, N., Delsol, C., Dragani, R., Fuentes, M., Geer, A. J., Haimberger, L., Healy, S. B., Hersbach, H., Hólm, E. V., Isaksen, L., Kållberg, P., Köhler, M., Matricardi, M.,

585 McNally, A. P., Monge-Sanz, B. M., Morcrette, J.-J., Park, B.-K., Peubey, C., de Rosnay, P., Tavolato, C., Thépaut, J.-N. and Vitart, F.: The ERA-Interim reanalysis: configuration and performance of the data assimilation system, Q.J.R. Meteorol. Soc., 137, 553-597, doi:10.1002/qj.828, 2011.

Dhomse, S. S., Emmerson, K. M., Mann, G. W., Bellouin, N., Carslaw, K. S., Chipperfield, M. P., Hommel, R., Abraham, N. L., Telford, P., Braesicke, P., Dalvi, M., Johnson, C. E., O'Connor, F., Morgenstern, O., Pyle, J. A., Deshler, T., Zawodny, J.
590 M., and Thomason, L. W.: Aerosol microphysics simulations of the Mt.Pinatubo eruption with the UM-UKCA composition-climate model, Atmos. Chem. Phys., 14, 11221–11246, doi:10.5194/acp-14-11221-2014, 2014.

Flower, V. J. B., and Kahn, R. A.: The evolution of Icelandic volcano emissions, as observed from space in the era of NASA's Earth Observing System (EOS), J. Geophys. Res. Atmos, 125, e2019JD031625, doi:10.1029/2019JD031625, 2020.

Gebhart, K. A., Schichtel, B. A., and Barna, M.G.: Directional biases in back trajectories caused by model and input data, J.
595 Air Waste Manage., 55, 1649-1662, doi:10.1080/10473289.2005.10464758, 2005.

Gettelman, A., Schmidt, A., and Egill Kristjánsson, J.: Icelandic volcanic emissions and climate, Nature Geosci., 8, 243, doi:10.1038/ngeo2376, 2015.

Gíslason, S. R., Stefánsdóttir, G., Pfeffer, M. A., Barsotti, S., Jóhannsson, Th., Galeczka, I., Bali, E., Sigmarsson, O., Stefánsson, A., Keller, N. S., Sigurdsson, Á., Bergsson, B., Galle, B., Jacobo, V. C., Arellano, S., Aiuppa, A., Jónasdóttir, E.
600 B., Eiríksdóttir, E. S., Jakobsson, S., Guðfinnsson, G. H., Halldórsson, S. A., Gunnarsson, H., Haddadi, B., Jónsdóttir, I., Thordarson, Th., Riishuus, M., Högnadóttir, Th., Dürig, T., Pedersen, G. B. M., Höskuldsson, Á., and Gudmundsson, M. T.: Environmental pressure from the 2014–15 eruption of Bárðarbunga volcano, Iceland, Geochem. Persp. Let. 1, 84-93, doi:10.7185/geochemlet.1509, 2015.

Grahn, H., von Schoenberg, P., and Brännström, N.: What's that smell? Hydrogen sulphide transport from Bardarbunga to
605 Scandinavia, J. Volcanol. Geoth. Res., 303, 187–192, doi:10.1016/j.jvolgeores.2015.07.006, 2015.

Gudmundsson, A., Lecoeur, N., Mohajeri, N., and Thordarson, T.: Dike emplacement at Bardarbunga, Iceland, induces unusual stress changes, caldera deformation, and earthquakes, Bull. Volcanol., 76, 1-7, doi:10.1007/s00445-014-0869-8, 2014.

Haghighatnasab, M., Kretzschmar, J., Block, K., and Quaas, J.: Impact of Holuhraun volcano aerosols on clouds in cloud-
610 system-resolving simulations, Atmos. Chem. Phys., 22, 8457–8472, doi:10.5194/acp-22-8457-2022, 2022.

Haywood, J. M., Jones, A., Clarisse, L., Bourassa, A., Barnes, J., Telford, P., Bellouin, N., Boucher, O., Agnew, P., Clerbaux, C., Coheur, P., Degenstein, D., and Braesicke, P.: Observations of the eruption of the Sarychev volcano and simulations using the HadGEM2 climate model, J. Geophys. Res., 115, D21212, doi:10.1029/2010JD014447, 2010.

Heaviside, C., Witham, C., and Vardoulakis, S.: Potential health impacts from sulphur dioxide and sulphate exposure in the
615 UK resulting from an Icelandic effusive volcanic eruption, Sci. Total Environ., 774, 145549, doi:10.1016/j.scitotenv.2021.145549, 2021.

Ialongo, I., Hakkarainen, J., Kivi, R., Anttila, P., Krotkov, N. A., Yang, K., Li, C., Tukiainen, S., Hassinen, S., and Tamminen, J.: Comparison of operational satellite SO2 products with ground-based observations in northern Finland during the Icelandic Holuhraun fissure eruption, Atmos. Meas. Tech., 8, 2279–2289, doi:10.5194/amt-8-2279-2015, 2015.

620 Ilyinskaya, E., Schmidt, A., Mather, T. A., Pope, F. D., Witham, C., Baxter, P., Jóhannsson, T., Pfeffer, M., Barsotti, S., Singh, A., Sanderson, P., Bergsson, B., Kilbride, B. M., Donovan, A., Peters, N., Oppenheimer, C., and Edmonds, M.: Understanding the environmental impacts of large fissure eruptions: Aerosol and gas emissions from the 2014–2015 Holuhraun eruption (Iceland), Earth Planet. Sci. Lett., 472. 309-322, doi:10.1016/j.epsl.2017.05.025, 2017.

Jordan, G.: Volcanic Aerosol-Cloud Interactions (VolcACI) Experiment: Part 1 Dataset, Zendo,
625 https://doi.org/10.5281/zenodo.7786775, 2023.

Keller, N., Stefani, M., Einarsdóttir, S. R., Helgadóttir, Á. K., Helgason, R., Ásgeirsson, B. U., Helgadóttir, D., Helgadóttir, I.
R., Tinganelli, L., Brink, S. H., Snorrason, A., and Þórsson, J.: National Inventory Report: Emissions of Greenhouse Gases in
Iceland from 1990 to 2020, The Environment Agency of Iceland: Reykjavík, Iceland, 2022.

de Leeuw, J., Schmidt, A., Witham, C. S., Theys, N., Taylor, I. A., Grainger, R. G., Pope, R. J., Haywood, J., Osborne, M.,
630 and Kristiansen, N. I.: The 2019 Raikoke volcanic eruption – Part 1: Dispersion model simulations and satellite retrievals of
volcanic sulfur dioxide, Atmos. Chem. Phys., 21, 10851–10879, doi:10.5194/acp-21-10851-2021, 2021.

Li, C., Krotkov, N. A., Carn, S., Zhang, Y., Spurr, R. J. D., and Joiner, J.: New-generation NASA Aura Ozone Monitoring
Instrument (OMI) volcanic SO_2 dataset: algorithm description, initial results, and continuation with the Suomi-NPP Ozone
Mapping and Profiler Suite (OMPS), Atmos. Meas. Tech., 10, 445–458, doi:10.5194/amt-10-445-2017, 2017.

635 Lund, M. T., Myhre, G., Haslerud, A. S., Skeie, R. B., Griesfeller, J., Platt, S. M., Kumar, R., Myhre, C. L., and Schulz, M.:
Concentrations and radiative forcing of anthropogenic aerosols from 1750 to 2014 simulated with the Oslo CTM3 and CEDS
emission inventory, Geosci. Model Dev., 11, 4909–4931, doi:10.5194/gmd-11-4909-2018, 2018.

McCoy, D. T., and Hartmann, D. L.: Observations of a substantial cloud–aerosol indirect effect during the 2014–2015
Bárðarbunga-Veiðivötn fissure eruption in Iceland, Geophys. Res. Lett., 42, 409–410,414, doi:10.1002/2015GL067070,
640 2015.

Malavelle, F. F., Haywood, J. M., Jones, A., Gettelman, A., Clarisse, L., Bauduin, S., Allan, R. P., Karset, I. H. H.,
Kristjánsson, J. E., Oreopoulos, L., Cho, N., Lee, D., Bellouin, N., Boucher, O., Grosvenor, D. P., Carslaw, K. S., Dhomse,
S., Mann, G. W., Schmidt, A., Coe, H., Hartley, M. E., Dalvi, M., Hill, A. A., Johnson, B. T., Johnson, C. E., Knight, J. R.,
O'Connor, F. M., Partridge, D. G., Stier, P., Myhre, G., Platnick, S., Stephens, G. L., Takahashi, H., and Thordarson, T.:
645 Strong constraints on aerosol–cloud interactions from volcanic eruptions, Nature, 546, 485–491, doi:10.1038/nature22974,
2017.

Neubauer, D., Ferrachat, S., Siegenthaler-Le Drian, C., Stier, P., Partridge, D. G., Tegen, I., Bey, I., Stanelle, T., Kokkola, H.,
and Lohmann, U.: The global aerosol–climate model ECHAM6.3–HAM2.3 – Part 2: Cloud evaluation, aerosol radiative
forcing, and climate sensitivity, Geosci. Model Dev., 12, 3609–3639, doi:10.5194/gmd-12-3609-2019, 2019.

650 NILU: EMEP manual for sampling and chemical analysis, Tech. rep., Norwegian Institute for Air Research, available at:
https:// projects.nilu.no//ccc/manual/index.html (last access: 6th January 2023), 2014.

NILU: EMEP data quality flags, Norwegian Institute for Air Research, available at: https://projects.nilu.no/ccc/flags/ (last
access: 6th January 2023), 2020.

Pattantyus, A. K., Businger, S., Howell, S. G.: Review of sulfur dioxide to sulfate aerosol chemistry at Kīlauea Volcano,
655 Hawai'I, Atmos. Environ., 185, 262–271, doi:10.1016/j.atmosenv.2018.04.055, 2018.Pedersen, G. B. M., Höskuldsson,
A., Dürig, T., Thordarson, T., Jonsdottir, I., Riishuus, M. S., Óskarsson, B. V., Dumonta, S., Magnusson, E., Gudmundsson,
M. T., Sigmundsson, F., Drouin, V. J. P. B., Gallagher, C., Askew, R., Gudnason, J., Moreland, W. M., Nikkola, P., Reynolds,
H. I., and Schmith, J.: Lava field evolution and emplacement dynamics of the 2014–2015 basaltic fissure eruption at
Holuhraun, Iceland, J. Volcanol. Geotherm. Res., 340, 155– 169, doi:10.1016/j.jvolgeores.2017.02.027, 2017.

660 Pfeffer, M., Bergsson, B., Barsotti, S., Stefánsdóttir, G., Galle, B., Arellano, S., Conde, V., Donovan, A., Ilyinskaya, E.,
Burton, M., Aiuppa, A., Whitty, R., Simmons, I., Arason, Þ., Jónasdóttir, E., Keller, N., Yeo, R., Arngrímsson, H.,
Jóhannsson, Þ., Butwin, M., Askew, R., Dumont, S., Löwis, S. von, Ingvarsson, Þ., La Spina, A., Thomas, H., Prata, F.,

Grassa, F., Giudice, G., Stefánsson, A., Marzano, F., Montopoli, M., and Mereu, L.: Ground-Based Measurements of the 2014–2015 Holuhraun Volcanic Cloud (Iceland), Geosciences, 8, 29, doi:10.3390/geosciences8010029, 2018.

665 Rayner, N. A., Parker, D. E., Horton, E. B., Folland, C. K., Alexander, L. V., Rowell, D. P., Kent, E. C., and Kaplan, A.: Global analyses of sea surface temperature, sea ice, and night marine air temperature since the late nineteenth century, J. Geophys. Res., 108, 4407, D14, doi:10.1029/2002JD002670, 2003.

Schmidt, A., Leadbetter, S., Theys, N., Carboni, E., Witham, C. S., Stevenson, J. A., Birch, C. E., Thordarson, T., Turnock, S., Barsotti, S., Delaney, L., Feng, W., Grainger, R. G., Hort, M. C., Höskuldsson, Á, Ialongo, I., Ilyinskaya, E., Jóhannsson, 670 T., Kenny, P., Mather, T. A., Richards, N. A. D., and Shepherd, J.: Satellite detection, long-range transport, and air quality impacts of volcanic sulfur dioxide from the 2014–2015 flood lava eruption at Bárðarbunga (Iceland), J. Geophys. Res. Atmos., 120, 9739– 9757, doi:10.1002/2015JD023638, 2015.

Schulz, M., Textor, C., Kinne, S., Balkanski, Y., Bauer, S., Berntsen, T., Berglen, T., Boucher, O., Dentener, F., Guibert, S. and Isaksen, I. S. A., Iversen, T., Koch, D., Kirkevåg, A., Liu, X., Montanaro, V., Myhre, G., Penner, J. E., Pitari, G., Reddy, 675 S., Seland, Ø., Stier, P., and Takemura, T.: Radiative forcing by aerosols as derived from the AeroCom present-day and pre-industrial simulations, Atmos. Chem. Phys., 6, 5225–5246, doi:10.5194/acp-6-5225-2006, 2006.

Sellar, A. A., Jones, C. G., Mulcahy, J. P., Tang, Y., Yool, A., Wiltshire, A., O'Connor, F. M., Stringer, M., Hill, R., Palmieri, J., Woodward, S., de Mora, L., Kuhlbrodt, T., Rumbold, S. T., Kelley, D. I., Ellis, R., Johnson, C. E., Walton, J., Abraham, N. L., Andrews, M. B., Andrews, T., Archibald, A. T., Berthou, S., Burke, E., Blockley, E., Carslaw, K., Dalvi, M., Edwards, J., 680 Folberth, G. A., Gedney, N., Griffiths, P. T., Harper, A. B., Hendry, M. A., Hewitt, A. J., Johnson, B., Jones, A., Jones, C. D., Keeble, J., Liddicoat, S., Morgenstern, O., Parker, R. J., Predoi, V., Robertson, E., Siahaan, A., Smith, R. S., Swaminathan, R., Woodhouse, M. T., Zeng, G., Zerroukat, M.: UKESM1: Description and evaluation of the U.K. Earth System Model, J. Adv. Model. Earth Syst., 11, 4513– 4558, doi:10.1029/2019MS001739, 2019.

Sigmundsson, F., Hooper, A., Hreinsdottir, S., Vogfjord, K. S., Ofeigsson, B. G., Heimisson, E. R., Dumont, S., Parks, M., 685 Spaans, K., Gudmundsson, G. B., Drouin, V., Arnadottir, T., Jonsdottir, K., Gudmundsson, M. T., Hognadottir, T., Fridriksdottir, H. M., Hensch, M., Einarsson, P., Magnusson, E., Samsonov, S., Brandsdottir, B., White, R. S., Agustsdottir, T., Greenfield, T., Green, R. G., Hjartardottir, A. R., Pedersen, R., Bennett, R. A., Geirsson, H., La Femina, P. C., Bjornsson, H., Palsson, F., Sturkell, E., Bean, C. J., Mollhoff, M., Braiden, A. K., and Eibl, E. P. S.: Segmented lateral dyke growth in a rifting event at Bárðarbunga volcanic system, Iceland, Nature, 517(7533), 191–195, doi:10.1038/nature14111, 2015.

690 Søvde, O. A., Prather, M. J., Isaksen, I. S. A., Berntsen, T. K., Stordal, F., Zhu, X., Holmes, C. D., and Hsu, J.: The chemical transport model Oslo CTM3, Geosci. Model Dev., 5, 1441–1469, doi:10.5194/gmd-5-1441-2012, 2012.

Steensen, B. M., Schulz, M., Theys, N., and Fagerli, H.: A model study of the pollution effects of the first 3 months of the Holuhraun volcanic fissure: comparison with observations and air pollution effects, Atmos. Chem. Phys., 16, 9745–9760, doi:10.5194/acp-16-9745-2016, 2016.

695 Stein, A. F., Draxler, R. R., Rolph, G. D., Stunder, B. J. B., Cohen, M. D., and Ngan, F.: NOAA's HYSPLIT atmospheric transport and dispersion modeling system, Bull. Am. Meteorol. Soc., 96, 2059–2077, doi:10.1175/BAMS-D-14-00110.1, 2015.

Stevens, B., Giorgetta, M., Esch, M., Mauritsen, T., Crueger, T., Rast, S., Salzmann, M., Schmidt, H., Bader, J., Block, K., Brokopf, R., Fast, I., Kinne, S., Kornblueh, L., Lohmann, U., Pincus, R., Reichler, T., and Roeckner, E.: Atmospheric 700 component of the MPI-M Earth System Model: ECHAM6, J. Adv. Model. Earth Sy., 5, 146–172, doi:10.1002/jame.20015, 2013.

Stewart, C., Damby, D. E., Horwell, C. J., Elias, T., Ilyinskaya, E., Tomašek, I., Longo, B. M., Schmidt, A., Carlsen, H. K., Mason, E., Baxter, P. J., Cronin, S., and Witham, C.: Volcanic air pollution and human health: recent advances and future directions, Bull. Volcanol., 84, 11, doi:10.1007/s00445-021-01513-9, 2022.

705 Takemura, T., Okamoto, H., Maruyama, Y., Numaguti, A., Higurashi, A., and Nakajima, T.: Global three-dimensional simulation of aerosol optical thickness distribution of various origins, J. Geophys. Res., 105, 17853–17873, doi:10.1029/2000JD900265, 2000.

Takemura, T., Nozawa, T., Emori, S., Nakajima, T. Y., and Nakajima, T.: Simulation of climate response to aerosol direct and indirect effects with aerosol transport-radiation model, J. Geophys. Res., 110, D02202, doi:10.1029/2004JD005029, 2005.

710 Takemura, T., Egashira, M., Matsuzawa, K., Ichijo, H., O'ishi, R., and Abe-Ouchi, A.: A simulation of the global distribution and radiative forcing of soil dust aerosols at the Last Glacial Maximum, Atmos. Chem. Phys., 9, 3061–3073, doi:10.5194/acp-9-3061-2009, 2009.

Tatebe, H., Ogura, T., Nitta, T., Komuro, Y., Ogochi, K., Takemura, T., Sudo, K., Sekiguchi, M., Abe, M., Saito, F., Chikira, M., Watanabe, S., Mori, M., Hirota, N., Kawatani, Y., Mochizuki, T., Yoshimura, K., Takata, K., O'ishi, R., Yamazaki, D., 715 Suzuki, T., Kurogi, M., Kataoka, T., Watanabe, M., and Kimoto, M.: Description and basic evaluation of simulated mean state, internal variability, and climate sensitivity in MIROC6, Geosci. Model Dev., 12, 2727–2765, doi:10.5194/gmd-12-2727-2019, 2019.

Tegen, I., Neubauer, D., Ferrachat, S., Siegenthaler-Le Drian, C., Bey, I., Schutgens, N., Stier, P., Watson-Parris, D., Stanelle, T., Schmidt, H., Rast, S., Kokkola, H., Schultz, M., Schroeder, S., Daskalakis, N., Barthel, S., Heinold, B., and Lohmann, U.: 720 The global aerosol–climate model ECHAM6.3–HAM2.3 – Part 1: Aerosol evaluation, Geosci. Model Dev., 12, 1643–1677, doi:10.5194/gmd-12-1643-2019, 2019.

Theys, N., De Smedt, I., Yu, H., Danckaert, T., van Gent, J., Hörmann, C., Wagner, T., Hedelt, P., Bauer, H., Romahn, F., Pedergnana, M., Loyola, D., and Van Roozendael, M.: Sulfur dioxide retrievals from TROPOMI onboard Sentinel-5 Precursor: algorithm theoretical basis, Atmos. Meas. Tech., 10, 119–153, doi:10.5194/amt-10-119-2017, 2017.

725 Toll, V., Christensen, M., Gassó, S., and Bellouin, N.: Volcano and ship tracks indicate excessive aerosol-induced cloud water increases in a climate model, Geophys. Res. Lett., 44, 492–412,500, doi: doi.org/10.1002/2017GL075280, 2017.

Tørseth, K., Aas, W., Breivik, K., Fjæraa, A. M., Fiebig, M., Hjellbrekke, A. G., Lund Myhre, C., Solberg, S., and Yttri, K. E.: Introduction to the European Monitoring and Evaluation Programme (EMEP) and observed atmospheric composition change during 1972–2009, Atmos. Chem. Phys., 12, 5447–5481, doi:10.5194/acp-12-5447-2012, 2012.

730 Twigg, M. M., Ilyinskaya, E., Beccaceci, S., Green, D. C., Jones, M. R., Langford, B., Leeson, S. R., Lingard, J. J. N., Pereira, G. M., Carter, H., Poskitt, J., Richter, A., Ritchie, S., Simmons, I., Smith, R. I., Tang, Y. S., Van Dijk, N., Vincent, K., Nemitz, E., Vieno, M., and Braban, C. F.: Impacts of the 2014–2015 Holuhraun eruption on the UK atmosphere, Atmos. Chem. Phys., 16, 11415–11431, doi:10.5194/acp-16-11415-2016, 2016.

Vignati, E., Wilson, J., and Stier, P.: M7: An efficient size-resolved aerosol microphysics module for large-scale aerosol 735 transport models, J. Geophys. Res., 109, D22202, doi:10.1029/2003JD004485, 2004.

Walker, J. C., Dudhia, A., and Carboni, E.: An effective method for the detection of trace species demonstrated using the MetOp Infrared Atmospheric Sounding Interferometer, Atmos. Meas. Tech., 4, 1567–1580, doi:10.5194/amt-4-1567-2011, 2011.

Walker, J. C., Carboni, E., Dudhia, A., and Grainger, R. G.: Improved detection of sulphur dioxide in volcanic plumes using
740   satellite-based hyperspectral infrared measurements: Application to the Eyjafjallajökull 2010 eruption, J. Geophys. Res., 117,
D00U16, doi:10.1029/2011JD016810, 2012.

Wells, A. F., Jones, A., Osborne, M., Damany-Pearce, L., Partridge, D. G., and Haywood, J. M.: Including ash in UKESM1
model simulations of the Raikoke volcanic eruption reveal improved agreement with observations, EGUsphere [preprint],
doi:10.5194/egusphere-2022-1060.

745   Williams, K. D., Copsey, D., Blockley, E. W., Bodas-Salcedo, A., Calvert, D., Comer, R., Davis, P., Graham, T., Hewitt, H.
T., Hill, R., Hyder, P., Ineson, S., Johns, T. C., Keen, A. B., Lee, R. W., Megann, A., Milton, S. F., Rae, J. G. L., Roberts, M.
J., Scaife, A. A., Schiemann, R., Storkey, D., Thorpe, L., Watterson, I. G., Walters, D. N., West, A., Wood, R. A.,
Woollings, T., Xavier, P. K.: The Met Office Global Coupled model 3.0 and 3.1 (GC3.0 and GC3.1) configurations, J. Adv.
Model. Earth Syst., 10, 357– 380, doi:10.1002/2017MS001115, 2017.

750   Witham, C., Kristiansen, N., Beckett, F., and Marenco, F.: Towards a global sulphur dioxide forecast capability for aviation,
Forecasting Research, Tech. Rep. No. 648, Met Office, 2021.